CrossMark

Teleconnection responses in multi-GCM driven CORDEX RCMs over Eastern Africa

Hussen Seid Endris[1] · Christopher Lennard[1] · Bruce Hewitson[1] · Alessandro Dosio[2] · Grigory Nikulin[3] · Hans-Jürgen Panitz[4]

Abstract The ability of climate models to simulate atmospheric teleconnections provides an important basis for the use and analysis of climate change projections. This study examines the ability of COordinated Regional climate Downscaling EXperiment models, with lateral and surface boundary conditions derived from Coupled Global Climate Models (CGCMs), to simulate the teleconnections between tropical sea surface temperatures and rainfall over Eastern Africa. The ability of the models to simulate the associated changes in atmospheric circulation patterns over the region is also assessed. The models used in the study are Rossby Centre regional atmospheric model (RCA) driven by eight CGCMs and COnsortium for Small scale MOdeling (COSMO) Climate Limited-area Modelling (COSMO-CLM or CCLM) driven by four of the same CGCMs. Teleconnection patterns are examined using correlation, regression and composite analysis. In order to identify the source of the errors, CGCM-driven regional climate model (RCM) results are compared with ERA-Interim driven RCM results. Results from the driving CGCMs are also analyzed. The RCMs driven by reanalysis (quasi-perfect boundary conditions) successfully capture rainfall teleconnections in most examined regions and seasons. Our analysis indicates that most of the errors in simulating the teleconnection patterns come from the driving CGCMs. RCMs driven by MPI-ESM-LR, HadGEM2-ES and GFDL-ESM2M tend to perform relatively better than RCMs driven by other CGCMs. CanESM2 and MIROC5, and their corresponding downscaled results capture the teleconnections in most of the sub-regions and seasons poorly. This highlights the relative importance of CGCM-derived boundary conditions in the downscaled product and the need to improve these as well as the RCMs themselves. Overall, the results produced here will be very useful in identifying and selecting CGCMs and RCMs for the use of climate change projecting over the Eastern Africa.

1 Introduction

Rainfall over Eastern Africa shows a high degree of inter- and intra-annual variability. This rainfall variability impacts the economy of the region because of the dependence of important sectors on rainfall (e.g. agriculture, water management, health and energy) and the relatively low adaptive capacity of these economies. For example, the two severe recent droughts 2008/2009 and 2011 in wide regions of Kenya, Ethiopia, Djibouti and Somalia affected food security and subjected millions of peoples to famine (FEWS NET 2011; Slim 2012; UNOCHA 2011). Previous studies have linked the interannual variability of rainfall over the region with sea surface temperature (SST) anomalies over the tropical Oceans (Ropelewski and Halpert 1987; Nicholson and Kim 1997; Clark et al. 2003; Behera et al. 2005).

✉ Hussen Seid Endris
hussen.seid1@gmail.com

[1] Climate System Analysis Group, University of Cape Town, Cape Town, South Africa

[2] European Commission Joint Research Centre, Institute for Environment and Sustainability, Ispra, Italy

[3] Rossby Centre, Swedish Meteorological and Hydrological Institute, Norrköping, Sweden

[4] Karlsruher Institut für Technologie, Institut für Meteorologie und Klimaforschung, Karlsruhe, Germany

Particularly, the El Niño Southern Oscillation (ENSO) (Ogallo 1988; Indeje et al. 2000; Mason and Goddard 2001; Segele et al. 2009a; Diro et al. 2011b) and the Indian Ocean Dipole (IOD) (Saji et al. 1999; Abram et al. 2008; Ummenhofer et al. 2009; Bahaga et al. 2015) are suggested to be the dominant drivers of the rainfall variability over the region. Thus, a better understanding of SST-rainfall teleconnections and their simulation by global and regional climate models (RCMs) is increasingly important to deliver reliable predictions of seasonal to interannual rainfall anomalies for disaster prevention (floods and droughts) and resource planning (agriculture, water and energy).

Global Climate Models (GCMs) are the primary tools for understanding the global climate and its projected change under different forcing scenarios (IPCC 2007, 2013). However, the coarse resolution of GCMs precludes them from capturing the effects of local forcings like terrain effects and land-sea contrasts that modulate the climate signal at finer scales (Giorgi et al. 2001; Wang et al. 2004; Rummukainen 2010). It also limits their ability to reproduce realistic extreme events that are critical to many users of climate information (Giorgi et al. 2009). In order to respond to the strategic, regional demands of society regarding climate variability and climate projection, various downscaling techniques have been developed. These are broadly categorized into statistical and dynamical downscaling techniques. Statistical downscaling develops robust statistical relationships between large-scale climate variables like atmospheric surface pressure and a local climate variable like rainfall at a particular place. This relationship is then mapped to GCM data to obtain the local variable response (Hewitson and Crane 1996). The main drawback of statistical downscaling is that it assumes the derived statistical relationship will not change due to climate change. On the other hand, dynamical downscaling involves the use of numerical models that simulate the climate over a chosen domain based on fundamental conservation laws and receives forcing GCM data at the domain boundaries. Dynamical downscaling include limited-area RCMs (e.g. Giorgi and Mearns 1991, 1999) and stretch-grid atmospheric GCMs (e.g. Déqué and Piedelievre 1995; Fox-Rabinovitz et al. 2006).

RCMs are widely used tool for climate process studies and climate change projection by using boundary conditions from reanalysis or GCMs output (Giorgi and Mearns 1999; Wang et al. 2004). By operating at high spatial resolutions, RCMs have the ability to capture small-scale features and process that influence the regional climate such as topographical influence and small-scale processes. However, accurate simulation of precipitation still remains a major challenge in RCMs as it depends on many processes. For example, Nikulin et al. (2012) show that precipitation is triggered too early during the diurnal cycle in

the majority of CORDEX RCMs. Endris et al. (2013) also show that most of the CORDEX models failed to reproduce the October–December (OND) rainfall peak over equatorial part of eastern Africa. Therefore, a process based comparison of models with observations is an important step to understand limitations of the models and to provide guidance for model improvement. Furthermore, the process based evaluation of models provides an important context for the interpretation and use of climate change projections. This is particulary important for CORDEX data users to explore the uncertainty for use of projected data.

Although several works have investigated the capability of RCMs to reproduce several features of African climatology (Segele et al. 2009b; Sylla et al. 2009; Paeth et al. 2011; Nikulin et al. 2012; Endris et al. 2013; Kalognomou et al. 2013 and Kim et al. 2014 among others), very few studies have attempted to evaluate the performance of RCMs in reproducing the large scale processes (e.g. teleconnections). Due to the high computational cost to run multiple RCMs and/or to force RCMs with output from a number of GCMs, those very few studies focused only on evaluating the performance of a single RCM driven by a single GCM and/or reanalysis datasets. For example, Anyah and Semazzi (2007) evaluated the capability of the International Center for Theoretical Physics RCM (ICTP-RegCM3) in reproducing the rainfall variability over east Africa and found that the model preserves the relationships between the regional rainfall and some of the global teleconnections (ENSO and IOD). Boulard et al. (2013) evaluated the performance of the Weather Research and Forecasting (WRF) model in downscaling large-scale climate variability over southern Africa with a particularly attention of ENSO. They showed limited skill in the model's ability to reproduce the seasonal droughts associated with El Ninõ conditions. Over tropical Americas, Tourigny and Jones (2009) evaluated the ability of the Rossby Centre Atmospheric Model (RCA) to downscale SST and large-scale atmospheric anomalies associated with ENSO, and found that the model reproduces the majority of the documented regional responses to ENSO forcing. However, it is well known that each model has its strengths and weaknesses depending on the season and region chosen for the analysis (e.g. Endris et al. 2013; Kalognoumou et al. 2013). Additionally, the boundary conditions provided to the RCMs plays an important role in the model's ability to propagate teleconnective signals into the region of interest. If the GCM is unable to capture, for example, the Walker circulation response to ENSO, it is unreasonable to expect the RCM to propagate the signal into the region of interest.

In this study, our aim is to examine the ability of two RCMs that participated in the COordinated Regional climate Downscaling EXperiment (CORDEX), with lateral and surface boundary conditions derived from reanalysis

and CGCMs, to accurately reproduce the observed spatiotemporal rainfall variability associated with the leading climate modes (like ENSO and IOD) affecting the eastern Africa on interannual time scales. We examine whether or not the downscaling propagates large-scale (teleconnective) forcing present in the reanalysis and CGCMs through the boundaries of the RCMs into the interior of the domain to simulate the local rainfall response. Such study is crucial since the capability of the RCMs to accurately simulate current climatic conditions associated with large-scale features constrains their ability to accurately simulate future climate. Obviously this idea is based on the assumption that current climate teleconnections with ENSO and IOD continue to operate in the same manner under a warming scenario. When RCMs are forced by CGCMs, the RCM simulations are affected by the combination effect of the imperfect driving fields and the RCMs' structural errors. Comparing reanalysis driven and CGCM-driven RCM results with observational data will help to determine whether errors come from the RCMs or driving lateral boundary conditions. To our knowledge, this is the first study assessing the ability of RCMs to simulate the climate impacts associated with ENSO and IOD over eastern Africa using different driving dataset as lateral boundary conditions.

The key research questions that we address in the study are:

1. Which oceanic basins have a strong relationship with Eastern Africa regional rainfall? This will be addressed using observed data.
2. How well the models perform at reproducing the observed teleconnection patterns (amplitudes and spatial patterns)?
3. How do different boundary forcings (from CGCMs) affect the RCM ability to simulate the teleconnections?
4. How well the models represent the anomalous circulation patterns associated with the leading climate modes affecting the rainfall over the region?

2 Data and methods

2.1 Study region and areas of analysis

The study region covers the Eastern Africa region (see Fig. 1). Because of the complexities of rainfall in the region, it is important to categorize the region into homogeneous rainfall subregions. As such we first classified the
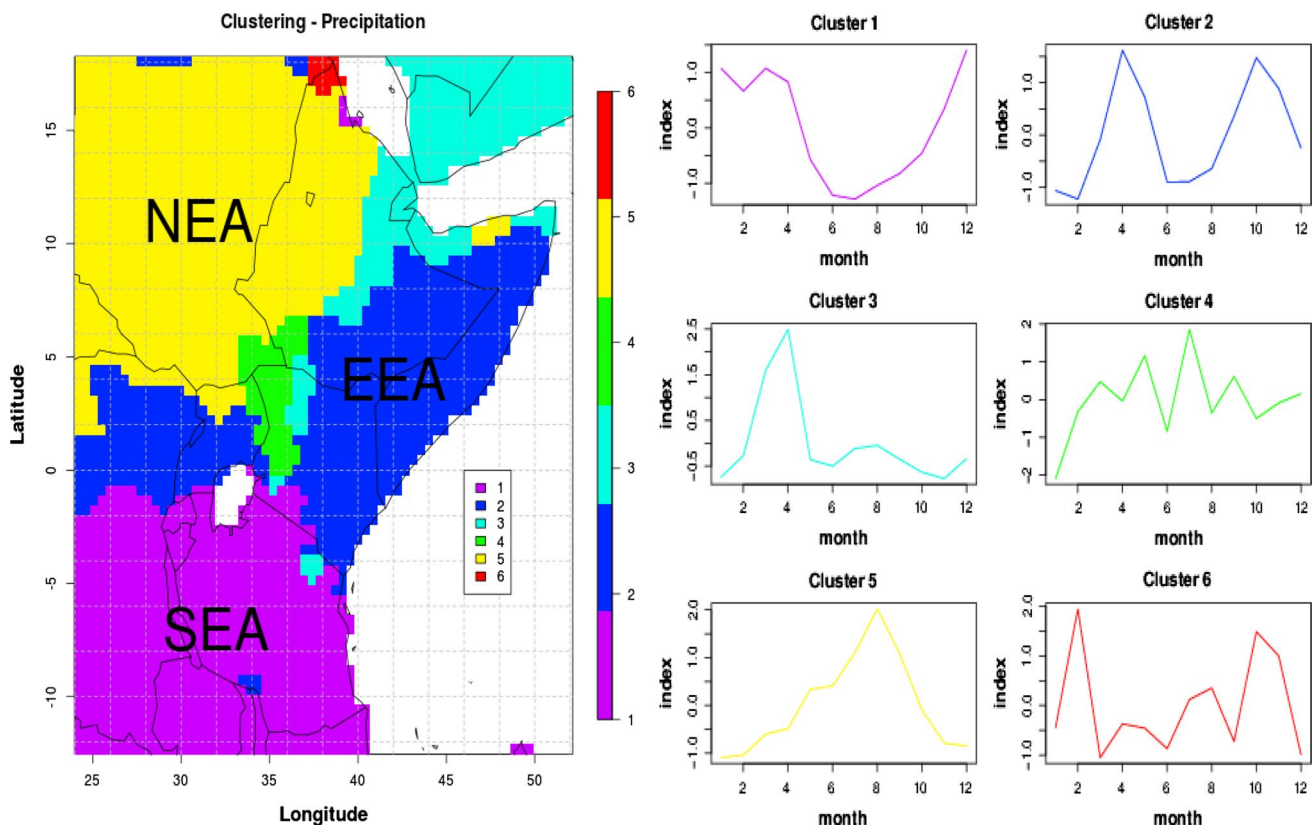

Fig. 1 Homogeneous rainfall regions (*left*) with corresponding annual cycles (*right*) as categorized using hierarchical agglomerative clustering technique

region into six climatically homogeneous rainfall subregions using Global Precipitation Climatology Centre data that has a spatial resolution of 0.5° (GPCC; version 5, 1901–2006; Rudolf et al. 2010). The regionalization was carried out using hierarchical agglomerative clustering technique with average linkage based on the R function *hclust* algorithms of Murtagh (1985). Like any other clustering methods, this method has its own limitations. One of the limitations of this technique is that it requires the analyst to specify the appropriate number of clusters. Since this study focuses on the large-scale forcings, and we also analyze coarse resolution GCM output, we choose to limit the number of clusters to six, however it should be noted that the number of homogeneous rainfall regions could be fewer or greater than this number depending on the objectives of the study. In fact, the result we obtained here is in agreement with previous studies conducted over different time periods using different observational data such as Liebmann et al. (2012) over Africa and Gissila et al. (2004) over Ethiopia.

Our analysis focuses on three subregions, which cover most of eastern Africa, namely: the northern part of Eastern Africa (NEA), Equatorial Eastern Africa (EEA) and the Southern part of Eastern Africa (SEA) (Fig. 1). NEA covers most the Ethiopian highlands and South Sudan, and some parts of Eritrea and Sudan, which has a rainfall maximum during boreal summer (June–September) and a pronounced dry season in boreal winter. EEA covers most of Somalia, Kenya, Uganda, and South Eastern parts of Ethiopia, and is characterized by a bimodal rainfall distribution with the major rainfall season in March–May (MAM) and a shorter rainfall season in October–December (OND). SEA lies south of the equator and is mainly characterized by long unimodal rainfall distribution extending from October to April.

The seasons analyzed in this study are JJAS for NEA, and OND for EEA and SEA. MAM rainfall season is not included in the analysis because rainfall teleconnections (i.e., correlations) with SSTs is much weaker (Indeje et al. 2000) and so is less usefully assessed against model data.

2.2 Data

2.2.1 Observed data

The observed rainfall dataset utilized in this study is the GPCC. This dataset is a gauge-based gridded observational dataset available at a 0.5° spatial and monthly temporal resolution. The observed SST data used in this study is the monthly mean National Oceanic and Atmospheric Administration Optimum Interpolation SST version 2 (NOAA_OI_SST_V2) gridded observational dataset, provided by the NOAA-CIRES Climate Diagnostics Center, Boulder,

USA (http://www.esrl.noaa.gov/psd/data/gridded/data.noaa.oisst.v2.html). The NOAA_OI_SST_V2 product integrates both in situ and satellite data from November 1981 to present at a 1° spatial resolution. These SST monthly fields are derived by a linear interpolation of the weekly optimum interpolation (OI) version 2 fields to daily fields and then averaging the daily values over a month (Reynolds et al. 2002). More details about the product can be found in Reynolds et al. (2002). Surface winds and sea level pressure dataset are based on ERA-Interim reanalysis (Dee et al. 2011). We note that reanalysis is essentially model simulations that incorporate all available observations at the time of the processing.

2.2.2 Model data

In this study we used the results from two CORDEX RCMs, namely the Rossby Centre regional atmospheric model (RCA) (Samuelsson et al. 2011) and COnsortium for Small scale MOdeling (COSMO) Climate Limited-area Modelling (COSMO-CLM or CCLM) [Baldauf et al. 2011]. Both models have first been run in an "evaluation" mode, i.e. driven by ERA-Interim for the period 1989–2008 (see Nikulin et al. 2012; Panitz et al. 2014). Thanks to SMHI institution, another RCA model evaluation run is performed and available for the period of 1980–2010. For the historical CGCM driven runs, which cover the period 1950–2005, RCA has been driven by 8 CGCMs and CCLM by 4 of the same CGCMs (see Dosio et al. 2015; Dosio and Panitz 2015 for CGCM driven CCLM runs). All the CORDEX Africa simulations were at spatial grid resolution of 0.44°. Table 1 presents a list of RCMs and driving CGCMs considered in the present study.

The CMIP5 CGCMs have different ensemble members (r1, r2, r3 etc.) different only in initial conditions around 1850, while the physics and the greenhouse gas forcing are the same. For CORDEX Africa simulations only the first member from the CMIP5 CGCMs is used to force the RCMs with the exception of the EC-EARTH model from which the 12th ensemble member was used. All CGCM and RCM rainfall data were interpolated to a common grid, similar to the observed GPCC dataset 0.5° resolution. As mentioned above, ERA-Interim driven RCA model run is available for the period of 1980–2010 as well as 1989–2008. We compared these two RCA evaluation runs with observation to check the sensitivity of teleconnection patterns to the choice of the period and found teleconnection patterns are not sensitive to the choice of the period. We therefore chose the 1989–2008 period for both RCM ERA-Interim downscalings as a common period. The CGCM and downscaled CGCM data were extracted from 1982 to 2005 to maximise the overlap with observed SST data to compute statistical relationships and quantify teleconective

Table 1 List of CORDEX RCMs and the driving CMIP5 CGCMs used

CGCMs	CGCMs Horizontal resolution	RCMs		Institute and country
		RCA	CCLM	
CNRM-CM5	$1.4° \times 1.4°$	✓	✓	CNRM, France
EC-EARTH	$1.125° \times 1.12°$	✓	✓	European Consortium
HadGEM2-ES	$1.875° \times 1.25°$	✓	✓	MOHC, United Kingdom
MPI-ESM-LR	$1.9° \times 1.9°$	✓	✓	MPI, Germany
CanESM2	$2.8° \times 2.8°$	✓		CCCma, Canada
GFDL-ESM2M	$2.5° \times 2.0°$	✓		NOAA/GFDL, United States
MIROC5	$1.4° \times 1.4°$	✓		CCSR/NIES/JAMSTEC, Japan
NorESM1-M	$2.5° \times 1.9°$	✓		NCC, Norway

RCA is driven by 8 CGCMs, while CCLM driven only by 4 CGCMs. All model dataset were obtained from the Earth System Grid Federation (ESGF) web portals

events. Although this period is not identical to that of the downscaled ERA-Interim runs, we again found that the assessment of teleconnection patterns were not sensitive to the choice of the period. Thus in all cases, our analysis focuses on the period of 1982–2005, with the exception of the ERA-Interim driven evaluation downscaling (1989–2008).

2.3 Methods

To assess the models' ability in representing teleconnection patterns, we follow an approach similar to Langenbrunner and Neelin (2013). Spearman's rank correlation and linear regression are used to calculate the seasonal precipitation teleconnections between regional rainfall and SSTs in a number of oceanic regions for the selected time period. The Spearman's rank-order correlation is a non-parametric rank statistic that measures the strength of the association between two variables (Hauke and Kossowski 2011). Unlike Pearson's product-moment correlation, it is a robust method in the presence of outliers, and does not require the assumption of normality. It also does not assume linear relationships, which means it is well-suited for exponential and logarithmic relationships. Linear regression is widely used for assessing the relationship between precipitation and SSTs. One limitation of this method is the assumption that precipitation data follow a Gaussian distribution, but in reality it is zero bounded and demonstrates non-gaussian behavior.

The analysis procedure is constructed in the following way. First, seasonal means have been computed for both precipitation and SST fields. Since teleconnection signals are the main focus of this study, long-term changes/trends were removed from both observed and simulation time series. Thus, all seasonal time series have been detrended linearly at each grid point. Each SST grid-point is then correlated against a spatially averaged rainfall time series to identify the oceanic regions that have robust relationships

with the regional seasonal rainfall, as well as to assess the models' ability to simulate the different patterns of teleconnections with each region. Once we have identified regions that have a strong relationship with regional rainfall, precipitation at each grid-point is regressed against a spatially averaged SST time series. The aim is to examine the ability of the model to capture the spatial pattern as well as the amplitude of the teleconnection patterns. Appropriate tests are used in the rank and linear methods to resolve grid-points that meet or pass 5 % significance level. Student's t test is used for computing the statistical significance for linear regression by assuming independent normal distributions. The statistical significance for the spearman's rank correlation is computed using z-test.

Finally, composite analysis is used to assess the models' ability to represent the anomalous circulation patterns associated to the dominant modes affecting the rainfall over the region. Details of this method are presented in section "d" under results and discussion part.

3 Results and discussion

Before analyzing how the climate models represent the teleconnection patterns, we first clarify two important points. The first point is that caution needs to be taken when comparing downscaled CGCMs climatologies (the historical runs) as a function of real calendar time, especially in relation to observational dataset. It is not expected the simulation of natural variability in downscaled CGCM simulations to follow the same time evolution as the observations. This is related with the experimental design of the driving CMIP5 CGCM simuations. The CMIP5 CGCMs are the so-called free-running simulations, and natural variability in these models is not constrained to occur in the same phase sequence as the real world (Taylor et al. 2012). In other words, there is no input to the models to control the natural or internal

variability in the simulated climate. To ensure the models to fellow the same phase with the simulated variability of the real world, the models either must be run in a forecast mode (i.e., models must be initialized to the current state of the coupled ocean–atmosphere system) (Yang et al. 2009) or in forced projection mode (i.e., models must be forced with observed SSTs) (Kosaka and Xie 2013). However, this is not the case for the CMIP5 CGCM runs. Therefore, like the driving CGCM simulations, it is not expected the simulated variability in downscaled CGCMs sequence to match in phase with reality. The models can still simulate the statistical properties of climate features. Thus, in our analysis for models driven by CGCMs, SST from the parent CGCM and rainfall from the RCMs is utilized to compute SST-rainfall teleconnections. However, for RCMs driven by reanalysis dataset, it is expected that the simulated variability occur temporally in phase with reality, so an observed SST dataset is used to analyze the teleconnection patterns. For the analysis of CGCM results, we use monthly precipitation and SST data from the CMIP5 CGCMs.

The second point concerns methods of assessing teleconnections for the multi-model ensemble mean. One approach, to obtain the teleconnection of ensemble mean, is by averaging the different model files to form a single file before computing the teleconnections, however, this is misleading as it smoothes the variability. Another approach is by calculating the teleconnections for each ensemble member (RCM realization) individually and average the patterns together later. While this is more widely used, obtaining a test of statistical significance becomes complicated, as one cannot easily take an average of significance tests across different models. A third approach (the option we have chosen) is by concatenating time series of the available models and then compute the teleconnection from the concatenated data as it allows computation of significant values. It is expected that too many significant correlations would emerge from this method, as there are a large number of observations as a result of the concatenation. To reduce the chances of obtaining erroneous/excessive significant correlations, an adjustment has been made to p values using Bonferroni correction (Bland and Altman 1995). Bonferroni correction is a statistical method used to correct p values when several dependent or independent statistical testes are being performed simultaneously on a single dataset. Accordingly, we obtained a new critical value for the concatenated data (**0.0125**) by deviding the critical p value (**0.05**) with the number of hypothsises being tested (**4**), with p value <0.0125 to be significant. We noted that apart from being able to obtain significant correlation in this approach, the teleconnection patterns obtained from the last two methods are almost identical.

Fig. 2 a Correlations of JJAS rainfall averaged over NEA, against ▶ concurrent grid-point SSTs. *Hatching* indicates regions where the correlation is statistically significant at the 5 % level. **b** Correlations of OND rainfall averaged over EEA, against concurrent grid-point SSTs. *Hatching* indicates regions where the correlation is statistically significant at the 5 % level. **c** Correlations of OND rainfall averaged over SEA; against concurrent grid-point SSTs. *Hatching* indicates regions where the correlation is statistically significant at the 5 % level

3.1 Teleconnection patterns resolved though Spearman rank correlation

In order to identify oceanic regions that have a robust relationship with regional rainfall and also to assess the models' ability to simulate the spatial pattern of the teleconnection, area averaged seasonal rainfall in each homogeneous rainfall subregion is correlated with concurrent grid point SSTs. These relationships are shown in Fig. 2a–c for the models and observation. In each case, the cross-hatches indicate statistically significant correlations at the 5 % level. Here significant correlations are computed using z-test statistic. The test statistics assumed to follow the normal distribution under the null hypothesis (i.e., no correlation). As has been mentioned above, RCA model was driven by 8 CGCMs, whereas CCLM was driven by 4 common CGCMs. For direct inter-comparison of CGCM and downscaled results, each Figure contains two panels (top and bottom). In the top panel, the first column shows the observational dataset, then the 4 common driving CGCMs and finally the CGCM ensemble mean; the second column shows the results of RCA driven by ERA-Interim, 4 common CGCMs and the ensemble mean; and the third column is similar to the second column, but for CCLM. In the bottom panel are the results of the remaining 4 CGCMs (first column) and the downscaled RCA results (second column).

Figure 2a shows the spearman's rank correlations between de-trended JJAS rainfall area-averaged over NEA, against de-trended concurrent grid-point SSTs. Hatching indicates statistically significant correlations at the 5 % level. The observed dataset (GPCC) shows that JJAS rainfall in the northern part of the region has significant correlation with SSTs in Eastern equatorial Pacific—a positive rainfall anomaly tends to occur during the cold phase of ENSO while dry conditions prevail during the warm phase ENSO. This is consistent with previous studies of Segele et al. (2009a) and Diro et al. (2011b), which use rain gauge rainfall data, and observed SST. This signal is also well captured by ERA-Interim driven RCMs. Mixed results are found in the CGCMs and the downscaled CGCM data. In some cases both CGCMs and corresponding downscaled results show similar teleconnection patterns, but in other cases the RCMs either deteriorate or improved the teleconnection signal. For example, EC-EARTH and MPI-ESM-LR and their corresponding downscaled results fail to
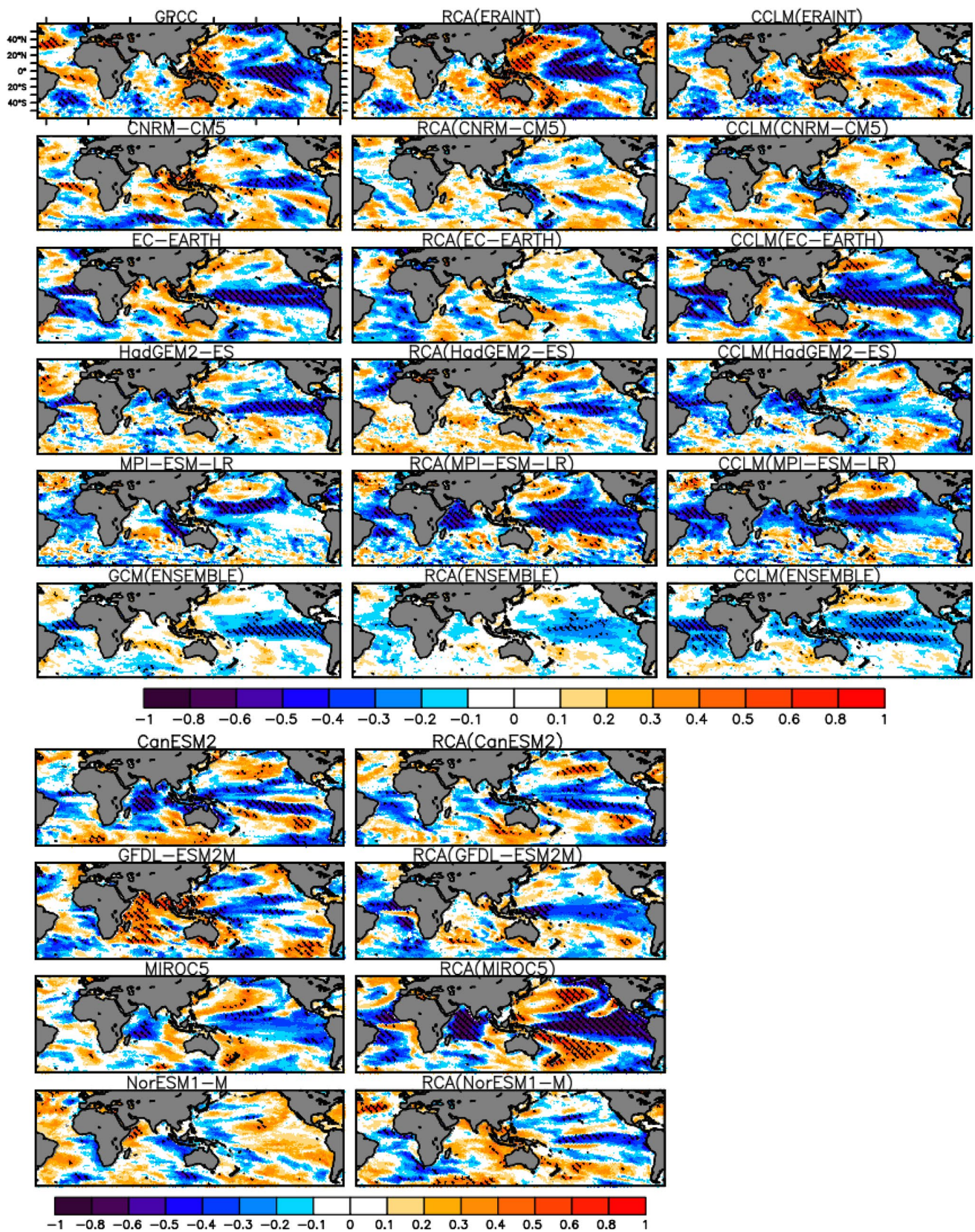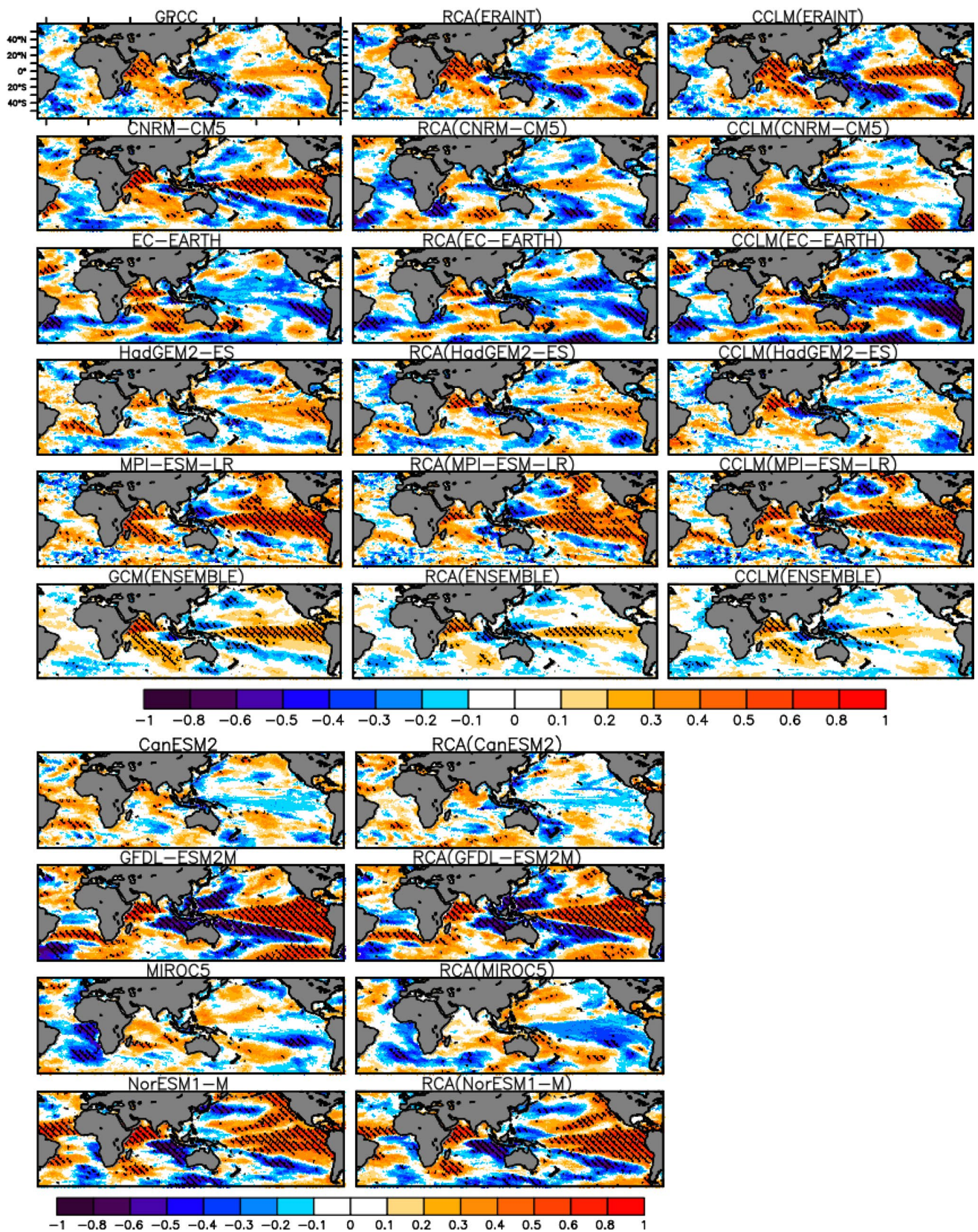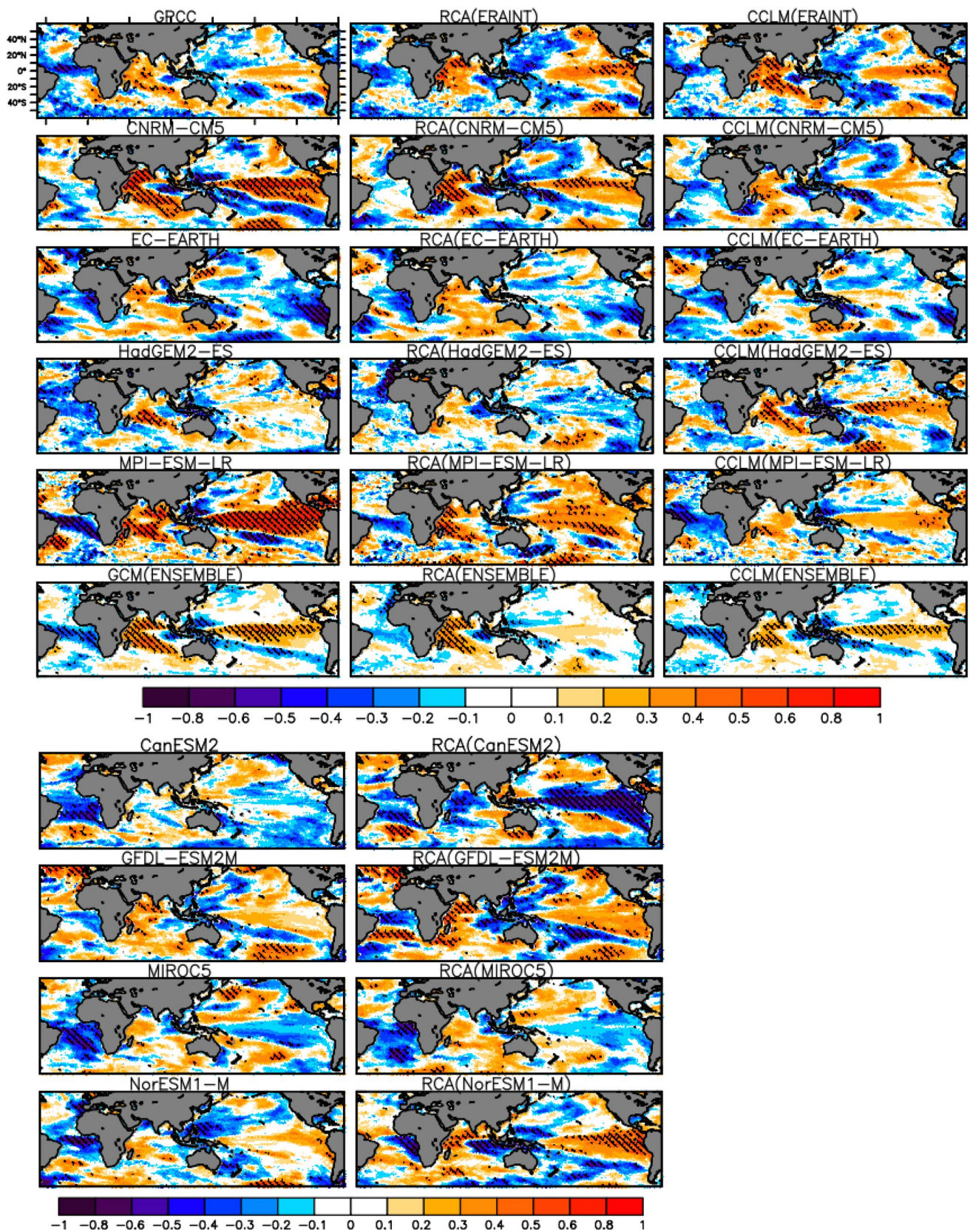
Fig. 2 continued

Fig. 2 continued

capture the positive correlation observed in our reference dataset (i.e., GPCC) over tropical Atlantic Ocean. Similarly, CanESM2, MIROC5 and corresponding downscaled results RCA (CanESM2) and RCA (MIROC5) show strong negative correlations with central Indian Ocean, which is not observed in our reference dataset. In those cases it is clear that the errors primarily originated from the driving CGCMs and the RCMs are unable to improve the teleconnection patterns. In few cases the RCMs deteriorated or improved the teleconnection patterns. For instance, NorESM1-M shows positive correlation with eastern equatorial pacific (which is opposite to the observed signal), while the downscaled result RCA (NorESM1-M) reproduced well the observed patterns. Similarly, GFDL-ESM2M shows strong positive correlations over the central Indian Ocean, whereas the corresponding downscaled result exhibit relatively good agreement with the observation (see Fig. 2a lower panel). These improvements in downscaled simulations might be due to the better representation of sub-GCM grid scale forcings by the RCM or because of the possible cancellation of errors produced by the RCM and those from the driving CGCM. Conversely, CNRM-CM5 captured the teleconnection with eastern equatorial Pacific Ocean, while the RCMs deteriorated the signal, especially RCA model.

Figure 2b represents the correlations between de-trended OND area-averaged rainfalls over EEA, against de-trended concurrent grid-point SSTs. During OND, warmer (colder) than average SSTs throughout the western Indian Ocean and equatorial Pacific Ocean are associated with enhanced (decreased) rainfall over the equatorial part of Eastern Africa. The correlations over the equatorial Pacific Ocean, however, are weaker compared to the western part of the Indian Ocean, and this suggest that the IOD is the dominant rainfall driver for the equatorial Eastern Africa region during OND. This is in agreement with the recent study of Bahaga et al. (2015) who indicated that the positive phase of IOD produces more rainfall (compared to the positive phase of ENSO) over the EEA by enhancing the moisture influx from Congo basin. The majority of the models, both CGCMs and the RCMs, simulated positive correlations between western Indian Ocean SST and the rainfall over EEA. Over all, the ERA-Interim driven downscaled results show better agreement with observed spatial teleconnection patterns than the CGCM driven downscaled results. It can be seen that disagreements exist in the CGCM downscaled results in reproducing the observed teleconnection patterns. The most notable feature is that EC-EARTH, CanESM2, MIROC5 and their downscaled results show opposite teleconnection patterns over Eastern equatorial Pacific Ocean. This clearly reflects the impact of the driving CGCM in producing a wrong signal in the downscaled results. MPI-ESM-LR, GFDL-ESM2M, NorESM1-M

and their corresponding downscaling results overestimate the strength of the teleconnections over Eastern equatorial Pacific. This overestimation in downscaled results are likely primarily associated with the respective driving CGCMs, however some error is attributable to the RCMs as ERA-Interim driven RCM simulations also overestimate the correlations over the equatorial Pacific Ocean. Unlike NEA (Fig. 2a), there is a similarity between the RCM results and their respective driving CGCM results in reproducing the teleconnection patterns in EEA (Fig. 2b).

Figure 2c is similar to Fig. 2b, but for SEA. Similar teleconnection patterns are observed as EEA, but the highest correlations are shifted to the central Indian Ocean instead of Western part of Indian Ocean and spatially there is less statistical significance in the correlations than the case of EEA. Despite this, we suggest that the central Indian Ocean is an important driver for the rainfall variability over SEA as suggested by Rowell (2013). Overall, the ERA-Interim driven RCM simulations captured the pattern and strength of teleconnections better than the CGCM-driven RCM simulations. CanESM2 and its corresponding simulation failed to reproduce the positive correlation over tropical Indian and Pacific Ocean. Similarly, MIROC5 and its corresponding downscaled result failed to represent the positive relationship between the SSTs over equatorial Pacific Ocean and rainfall over SEA. This again reflects the effect of boundary conditions for the wrong teleconnections in the downscaled results.

It is worth noting that the teleconnections between SSTs and rainfall over EEA and SEA (Fig. 2b, c) are generally very similar in the CGCM simulations and their downscaled results than the case of NEA (Fig. 2a). This might be related with the processes that drive the seasonal rainfall in the respective regions. As suggested by previous studies (Indeje et al. 2000), OND rainfall over EEA and SEA is mainly controlled by large-scale features, while both local and large-scale features control JJAS rainfall over NEA (Diro et al. 2011a; Endris et al. 2013). Thus it is expected that a discrepancy might exist between the RCM and the respective driving CGCM simulations over a region where mesoscale processes have important influence on rainfall, as the CGCMs cannot adequately represent small-scale features.

It is also important to mention that the similarity between the downscaled ERA-Interim and the observed patterns is much greater than the similarity between the downscaled CGCM and the original CGCM patterns (Fig. 2a–c). We further assess this by analyzing and comparing the deviation of the reanalysis-driven teleconnection patterns from observation and/with deviation of CGCM-driven simulations from the CGCMs (not shown). The results show that the RCMs change teleconnection patterns from CGCMs much more than they change patterns when driven by reanalysis dataset. This is particularly true over

Fig. 3 Pattern correlation of correlation coefficients between the models and observation **a** over NEA (JJAS), **b** EEA (OND) and **c** SEA (OND). Correlations are weighted with respect to latitude
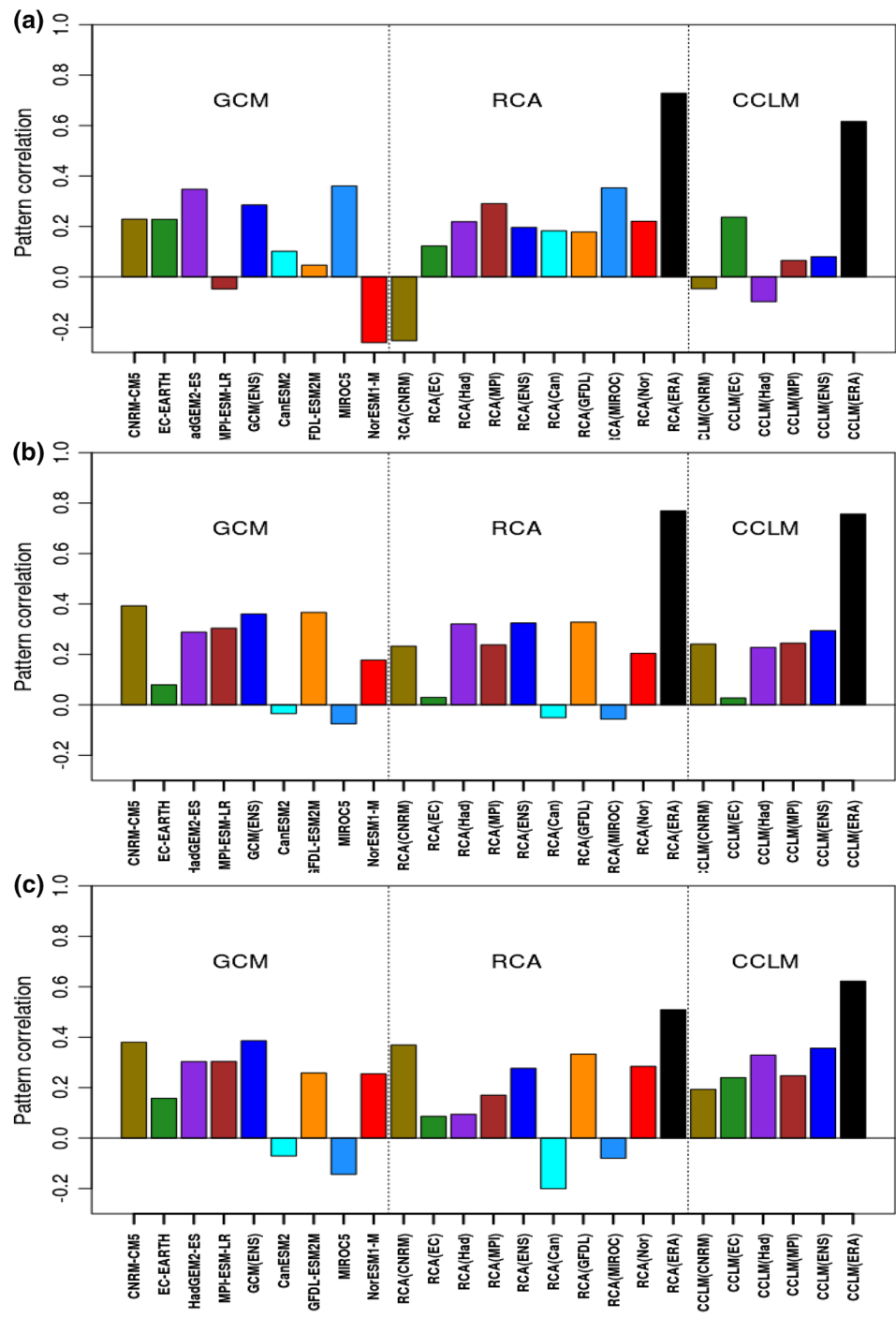
topographically complex region (NEA) where the local rainfall is controlled by both mesoscale and large-scale processes. As noted above, the interaction between small-scale and large-scale features might cancel out or increase the noise when downscaled if there are unrealistic features in the driving fields of the CGCM.

It is, however, difficult to assess the individual model performance since some models capture some teleconnections but not others. Thus an objective and quantitative approach is applied by calculating the spatial (pattern) correlation of temporal correlations. Figure 3 represents the pattern correlation of correlation coefficients between observation and each model. Due to the curvature of the Earth, the actual area represented by a latitude/longitude grid sample decreases with latitude. Thus, to ensure that each grid point is weighted by the area it represents, the correlation values at each grid-point are multiplied by the square root of the cosine of latitude.
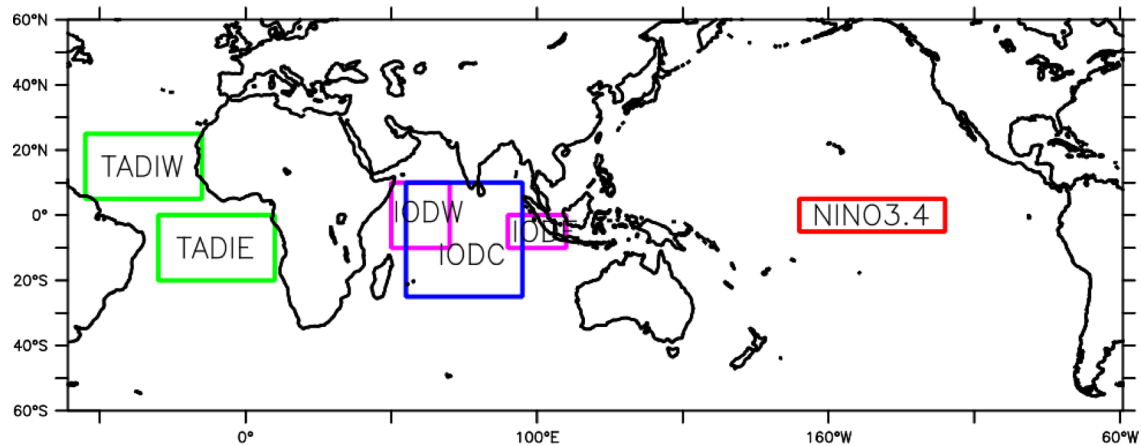
1. NINO3.4 index - average of 5°S–5°N, 170°–120°W

2. IOD - averages of 10°S–10°N, 50°–70°E minus 10°S–0°, 90°–110°E

3. IODC - average of 25°S–10°N, 55°–95°E

4. TADI - averages of 5°–25°N, 55°–15°W minus 20°S–0°, 30°W–10°E

Fig. 4 Location of SST regions used to compute indices in the analysis

The ERA-Interim driven RCM runs perform better than any CGCM runs in reproducing the spatial pattern of teleconnections in every subregion and season, but again there is a wide disagreement in CGCM-driven RCMs between one another and with the observation. There is also no clear improvement by the RCMs of their driving CGCM results. For example, over NEA during JJAS (Fig. 3 top panel), CNRM-CM5 shows a positive pattern correlation with the observed GPCC, but its corresponding downscaled results (both by RCA and CCLM model) show negative pattern correlation i.e. RCMs have deteriorated the teleconnection relationship. In contrast, NorESM1-M and MPI-ESM-LR show a negative correlation, while their downscaled results improve the correlation. Over EEA and SEA during OND (Fig. 3 middle and bottom panel), HadGEM2-ES, MPI-ESM-LR, GFDL-ESM2M and Ensemble Mean captured the pattern correlation better than any other models, while CanESM2 and MIROC5 performed poorly. As it was discussed earlier, there is a similarity between the RCM simulations and their driving CGCMs simulations in reproducing the spatial pattern of teleconnections over EEA and SEA during OND.

In general, results from the correlation analysis have shown that ENSO has a strong association with rainfall over the northern part of the region during JJAS, while the effect of IOD is more evident for equatorial and southern part of the region during OND. It is also clear that the ERA-Interim driven RCMs outperform the CGCM-driven RCMs, suggesting that boundary conditions from the CGCM are indeed is the main contributor to poor skill in

representing the response to teleconnections in the RCMs. It is also worth mentioning that similarities in SST-rainfall teleconnection patterns between the RCM simulations and respective driving CGCM simulations are noticeable over regions where the rainfall is primarily controlled by large-scale (synoptic-scale) features, with the RCM simulations conserving the overall regional patterns from the forcing models. Differences in RCM simulations from corresponding driving simulations are noted mainly over northern part of the domain which is most likely related to mesoscale processes that are not resolved by CGCMs.

3.2 Teleconnection pattern resolved through linear regression

To evaluate the ability of individual models to simulate both the patterns and amplitude of rainfall teleconnections, a regression analysis was applied to SST indices in Oceanic regions that have strong correlations with eastern African rainfall. The SST regions used to compute indices are indicated in Fig. 4. These regions have been selected based on Fig. 2a–c and literatures that describe the relationship between Eastern Africa rainfall and SST (e.g. Ogallo 1988; Saji et al. 1999; Ummenhofer et al. 2009; Diro et al. 2011b; Rowell 2013). For the Pacific, the **NINO3.4 index,** which is the average of SST over 5°S–5°N, 170°–120°W, is used to measure ENSO variability. For the Indian Ocean, we use the standard definition of IOD (Saji et al. 1999), which is the difference between the area average SST in the IODW region (10°S–10°N, 50°–70°E) and IODE region (10°S–0°,

90°–110°E). Also the central Indian Ocean Index **(CIOD)**, which is the average of SST over 25°S–10°N, 55°–95°E, is used following Rowell (2013). In the Atlantic, a Tropical Atlantic Dipole Index (**TADI**) is defined as the difference between tropical North and South Atlantic indices (averages of 5°–25°N, 55°–15°W minus 20°S–0°, 30°W–10°E), following Enfield et al. (1999).

As discussed earlier, the main advantage of using regression over the Spearman rank correlation is that we can interpret the teleconnections in terms of changes in the magnitude of the physical variables, which in this case is rainfall rate per degree change of SST in the different ocean regions. It is important to note that linear regression makes a few assumptions about the data (e.g. linearity and normality). Thus we checked the sensitivity of teleconnection patterns to the statistical assumptions going into the calculations with Spearman's rank method, which does not make such assumptions (Fig not shown). The test confirmed that teleconnection patterns are not sensitive to the statistical methods employed. As has been noted by Langenbrunner and Neelin (2013), teleconnection patterns defined with linear regression are useful for questions that involve the amplitude of the signal.

Figures 5a shows observed and modeled rainfall teleconnections for the JJAS season against NINO3.4 as estimated by linear regression. Stippled patterns indicate statistically significant regression coefficients at the 5 % level. Here student's t-test is used to resolve grid points that meet or pass 5 % significance level. The test statistics assumed to follow the t-distribution under null hypothesis regression slop of zero. Negative coefficients occur over most of the northern part of the domain indicating that rainfall is above normal when the index is negative, and the rainfall is below normal when the index is positive. The majority of models reproduce these observed features. Both RCMs driven by CNRM-CM5 poorly simulate the teleconnection patterns against Niño3.4 index, while driving CGCM (CNRM-CM) reproduced the pattern better than the downscaled results. GFDL-ESM2M and NorESM1 produced wrong signal over the northern part of the domain. The regression coefficients between JJAS rainfall and TADI were also calculated (not shown). The results show that TADI has week and localized effect over the region during JJAS compared to the influence of ENSO, and there is a disagreement among the models in capturing the teleconnections patterns.

Rainfall teleconnections for the OND season against NINO3.4 and IOD index estimated by linear regression are indicated in Fig. 5b, c, respectively. Both indices have a positive relationship with the regional rainfall, but the IOD rainfall relationships are stronger than the ENSO rainfall relationships, and this indicates the influence of the IOD on regional rainfall during OND is higher than ENSO. The majority of the models reproduced the teleconnection against both indices. Once again there is a clear effect of

the CGCM-supplied boundary conditions in simulating the teleconnection patterns. For example, the wrong signal in EC-EARTH, CanESM2 and MIROC5 over NINO3.4 region resulted in wrong teleconnection patterns in their corresponding downscaled results (Fig. 5b). Similarly, the wrong teleconnection signal in CanESM2 and MIROC5 models against IOD affected the teleconnection in their downscaled results (Fig. 5c).

To understand the effect of the central Indian Ocean over the region, regression coefficients between OND rainfall and CIOD were calculated (not shown). The CIOD has a large influence in the southern region of the domain with excess (deficit) rainfall being associated with warming (cooling) of the central Indian Ocean as shown by Rowell (2013). Like the case of ENSO and IOD, differences in regional simulations associated with the CIOD originate mainly from the respective CGCM fields (not shown).

Figure 5a–c provide a spatial assessment of teleconnection patterns over the entire Eastern Africa region, and one can see that there is often disagreement between the CGCMs as well as the downscaled results in different regions. We further assess and summarize the ability of the models to reproduce the spatial pattern of teleconnections and represent the amplitude of these patterns in each homogeneous rainfall sub-regions using Taylor diagrams (Taylor 2001). The Taylor diagrams in Fig. 6 show the spatial root mean square deviation and spatial correlation of regression field (i.e. regression coefficients from Fig. 5a–c, and regression coefficients against TADI and CIOD discussed previously) of models with respect to the reference field in each homogeneous rainfall sub-regions. The spatial root mean square deviations (spatial standard deviation) of the models are normalized against the spatial standard deviation of the observation, and this spatial standard deviation is used as a measure of the teleconnection amplitudes. Examination of spatial patterns of teleconnections based on pattern correlation demonstrated that similarties between the regional simulations and the respective CGCM simulations are evident, with the RCM simulations maintaining the regional patterns from the forcing models. Concering the amplitude of teleconnections, CGCMs generally tend to underestimate the amplitude, while the RCMs overestimate it in most of the subregions against the different indices (Fig. 6a, b). The high amplitude of teleconnection (i.e., higher spatial standard deviation) in the RCM simulations might be directly due to better precipitation capture, enhanced by a better-resolved topography. On the other hand, the low amplitude of teleconnection in CGCMs may be assocaited with a poorly resolved topography and other small-scale features due to coarse resolution. The other possibility for the discrepancy of the amplitude was likely due to the interpolation as we re-gridded the coarse resolution data to a higher resolution (0.44°). However, re-gridding the high resolution dataset into coarse resolution (2°) gave nearly identical results.
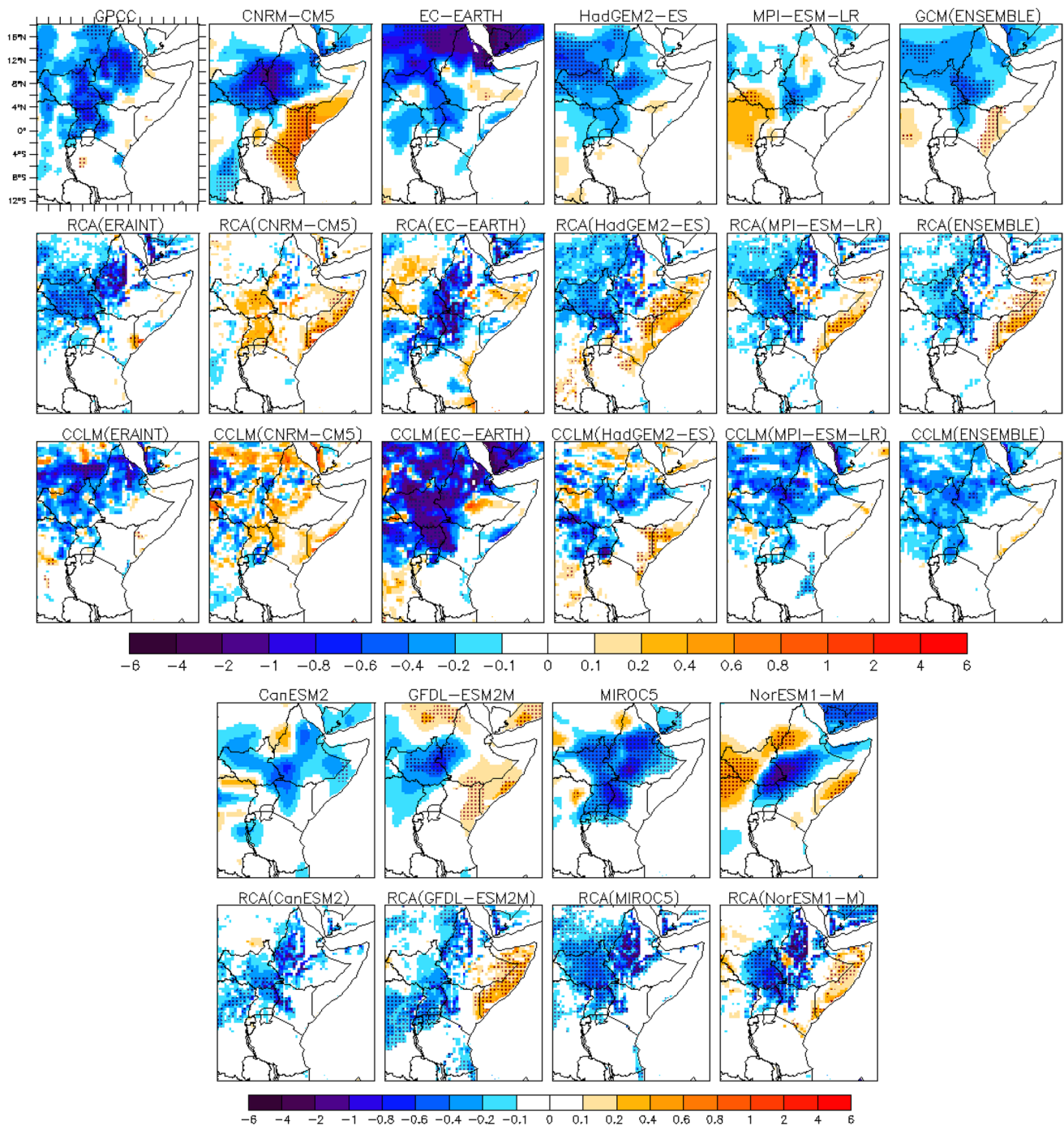
JJAS - NINO3.4 index

Fig. 5 **a** JJAS rainfall teleconnections, as diagnosed through a linear regression analysis of rainfall against the Nino3.4 index. *Stippling* indicates regions where the regression coefficient is statistically significant at the 5 % level. Units are mm day^{-1} °C^{-1}. **b** OND rainfall teleconnections, as diagnosed through a linear regression analysis of rainfall against the Nino3.4 index. *Stippling* indicates regions where

the regression coefficient is statistically significant at the 5 % level. Units are mm day^{-1} °C. **c** OND rainfall teleconnections, as diagnosed through a linear regression analysis of rainfall against the IOD. *Stippling* indicates regions where the regression coefficient is statistically significant at the 5 % level. Units are mm day^{-1} °C^{-1}
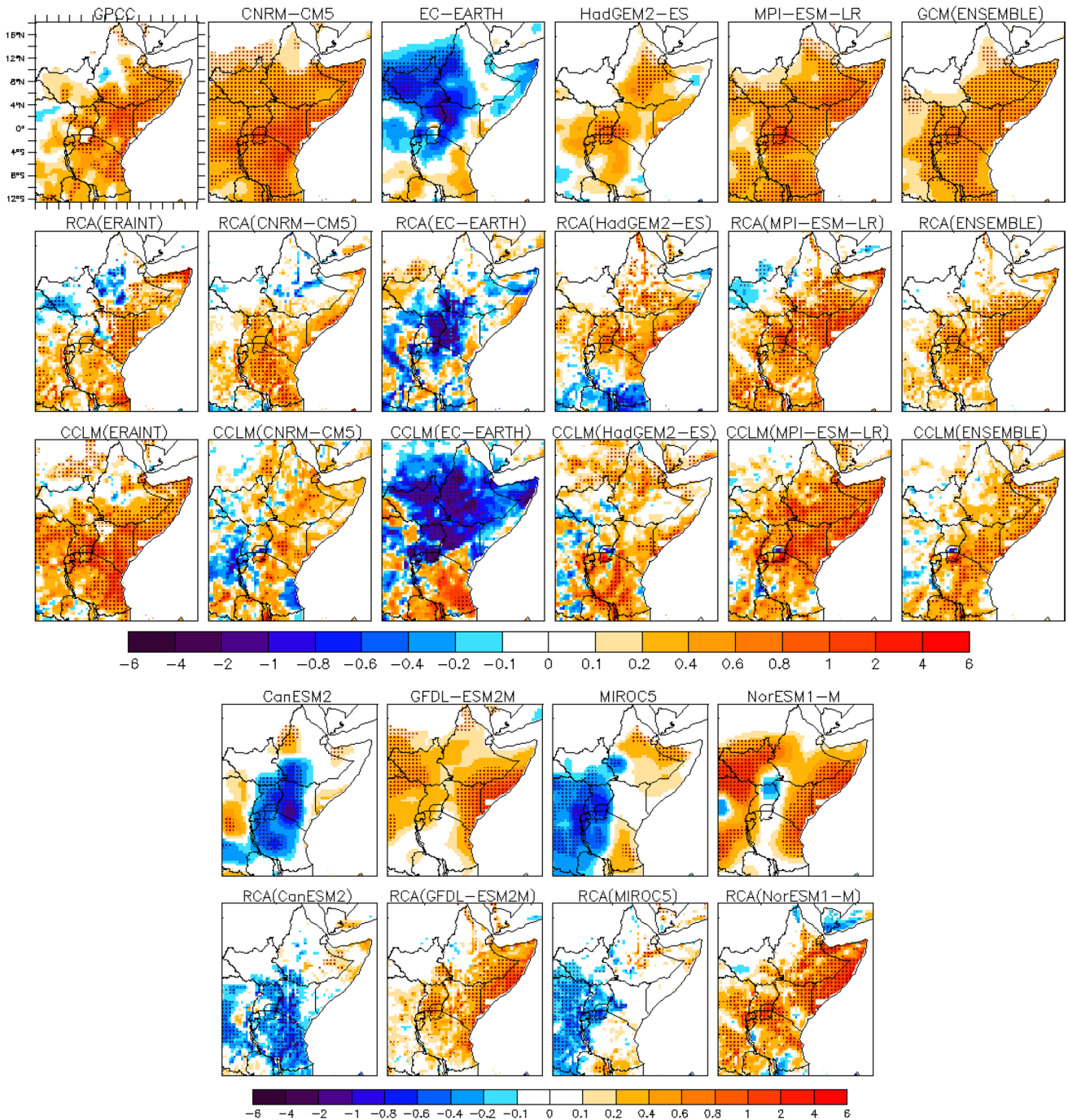
OND - NINO3.4 index

Fig. 5 continued

3.3 Simulating mean climate

Finally, we evaluated the models' performance for simulating the mean climate to check if there is straightforward relationship to their performance in capturing the teleconnections. Taylor diagrams are used to

compare model performance for the annual cycle of rainfall with observation in each homogeneous rainfall sub-regions (Fig. 7). Overall, the models produce better annual cycles of rainfall in NEA and SEA (over uni-model rainfall regions) than in EEA (bi-model rainfall region). The ERA-Interim driven RCMs reproduce

OND - IOD index
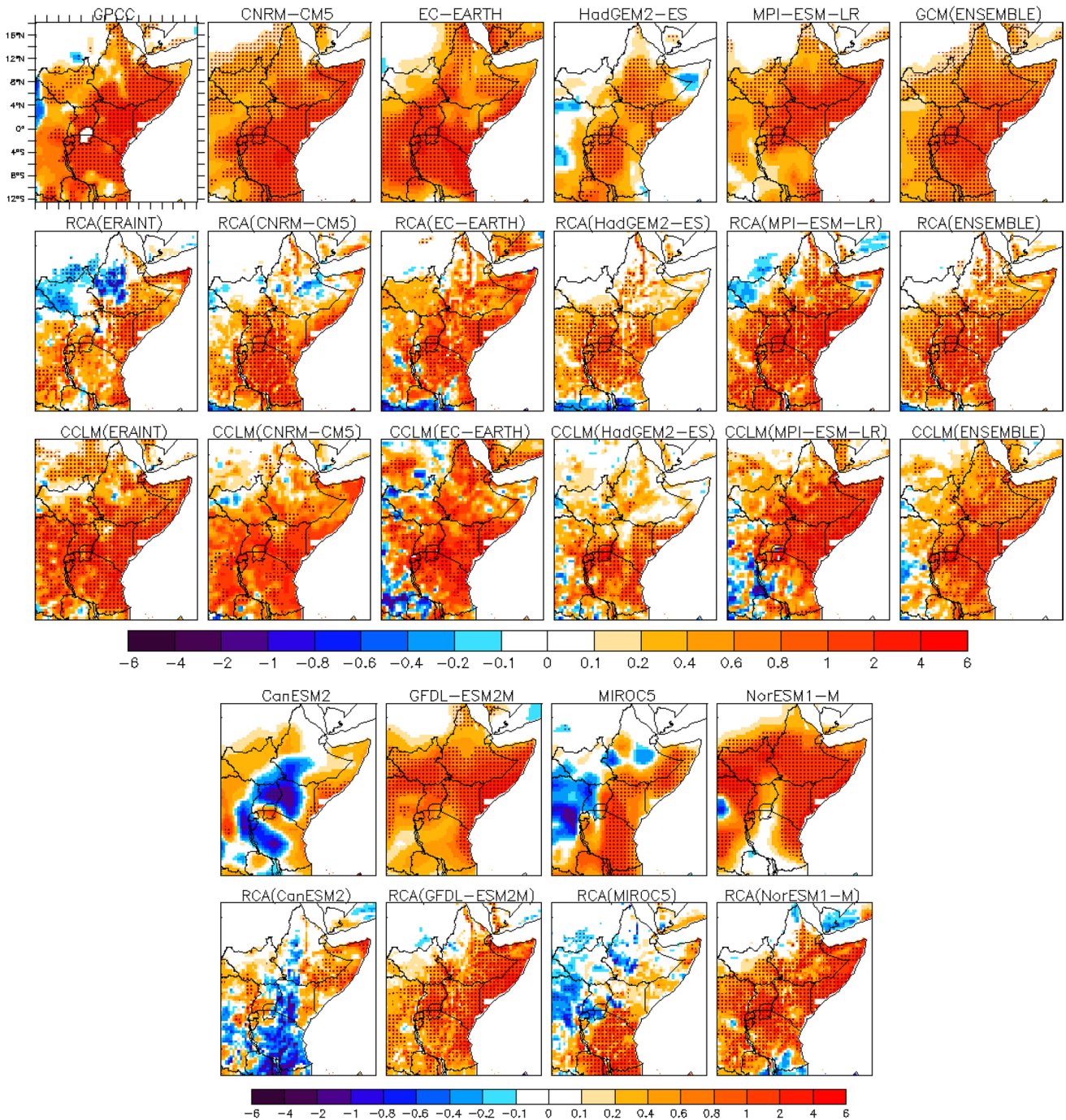
Fig. 5 continued

the annual cycles better than CGCM driven RCMs and parent CGCMs. GFDL-ESM2 and NorESM1-M poorly reproduce the annual cycle in NEA (i.e. correlations less than 0.8). HadGEM2-ES, GFDL-ESM2M, NorESM1-M and their corresponding downscaled results are among poorly performing models in EEA. CanESM2, MIROC5,

NorESM1-M and GFDL-ESM2M overestimate the standard deviation over SEA, while CNRM-CM5 underestimates it. From these figures it appears that the ability of the models in reproducing the teleconnections is not directly related to their ability in representing the climatological rainfall pattern.
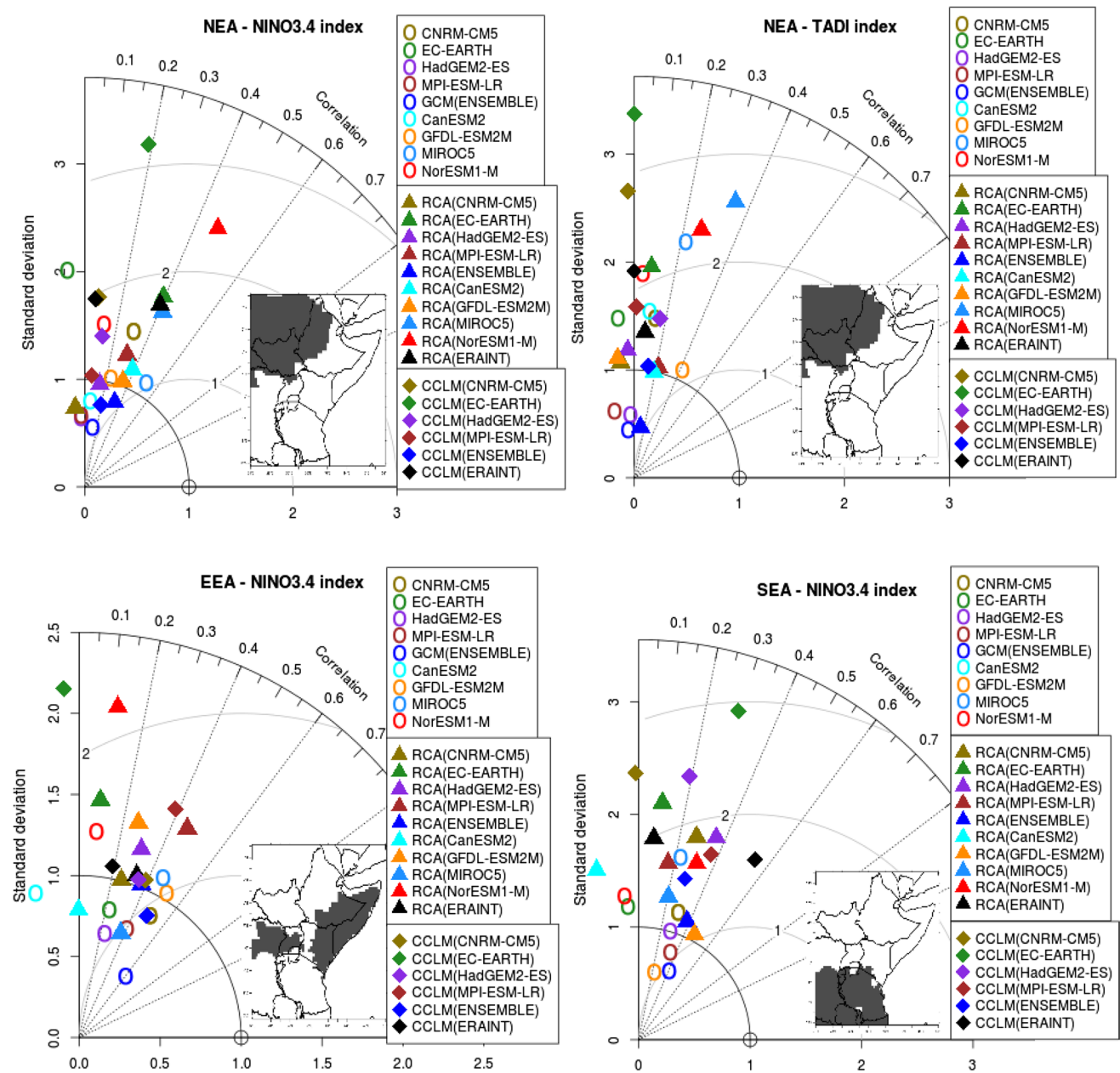
Fig. 6 a Taylor diagrams for the standardized amplitude and spatial correlation of precipitation teleconnections in NEA during JJAS against NINO3.4 (*top left*), NEA during JJAS against TADI (*top right*), EEA during OND against NINO3.4 (*lower left*) and SEA during OND against NINO3.4 (*bottom right*). On the Taylor diagrams, *angular axes* show spatial correlations between modeled and observed teleconnections; *radial axes* show spatial standard deviation (root-mean-square deviation) of the teleconnection signals in each area, normalized against that of the observations. *Circles* are for GCMs, triangles are for RCA and diamonds for CCLM model. **b** Tay-

lor diagrams for the standardized amplitude and spatial correlation of OND rainfall teleconnections in EEA against IOD (*top left*), EEA against CIOD (*top right*), SEA against IOD (*lower left*) and SEA against CIOD (*lower right*). On the Taylor diagrams, *angular axes* show spatial correlations between modeled and observed teleconnections; *radial axes* show spatial standard deviation (root-mean-square deviation) of the teleconnection signals in each area, normalized against that of the observations. *Circles* are for GCMs, triangles are for RCA and diamonds for CCLM model

3.4 Circulation anomalies

Composite analysis is used to assess the ability of the models to represent key regional anomalous atmospheric circulation patterns associated with ENSO and IOD variability. ENSO and IOD years are identified from each CGCM and observation, by calculating the Oceanic Niño Index (ONI) and Dipole Mode Index (DMI), respectively.
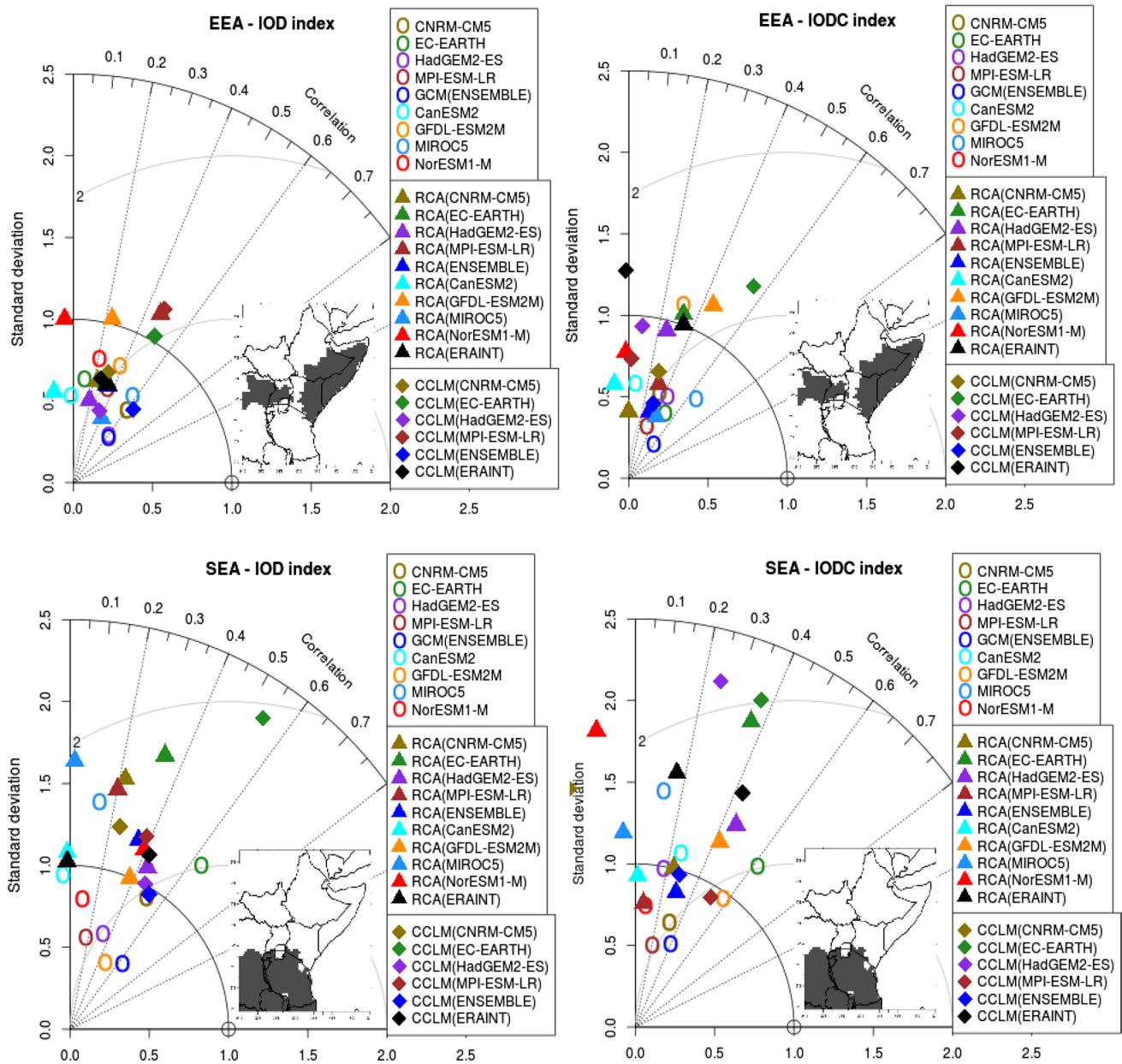
Fig. 6 continued

To identify the ENSO years, we follow an approach similar to da Rocha et al. (2014). The ONI based on the SST anomaly in Niño3.4 region (120°–170°W and 5°S–5°N) is used to identify El Niño and La Niña years. Here the anomaly is calculated relative to a climatological seasonal cycle based on the years 1982–2005. A given year is defined as El Niño or La Niña year when ONI value is higher (lower) than a positive (negative) threshold for at least five consecutive overlapping seasons, defined as the average of three consecutive months of that year. The NOAA Climate Prediction Center (CPC) uses a threshold of ±0.5 °C, while here, similar to da Rocha et al. (2014), the CGCM

thresholds are based on their respective ONI standard deviation (Sd). The reason is that some models might show excessive number of El Niño and La Niña years due to the high Sd in Niño3.4 region if a ±0.5 °C threshold is used.

The CGCMs' thresholds for El Niño and La Niña are defined by the following criteria:

$$T_i = Sd_i * C$$

T_i is the threshold of the ith CGCM Sd_i is the ONI Sd of the ith CGCM C is a constant (or fixed value) = 0.47, which is the ratio between a threshold used by CPC (**±0.5**) and ONI Sd from NOAA for the period of 1982–2005 (**1.07**).
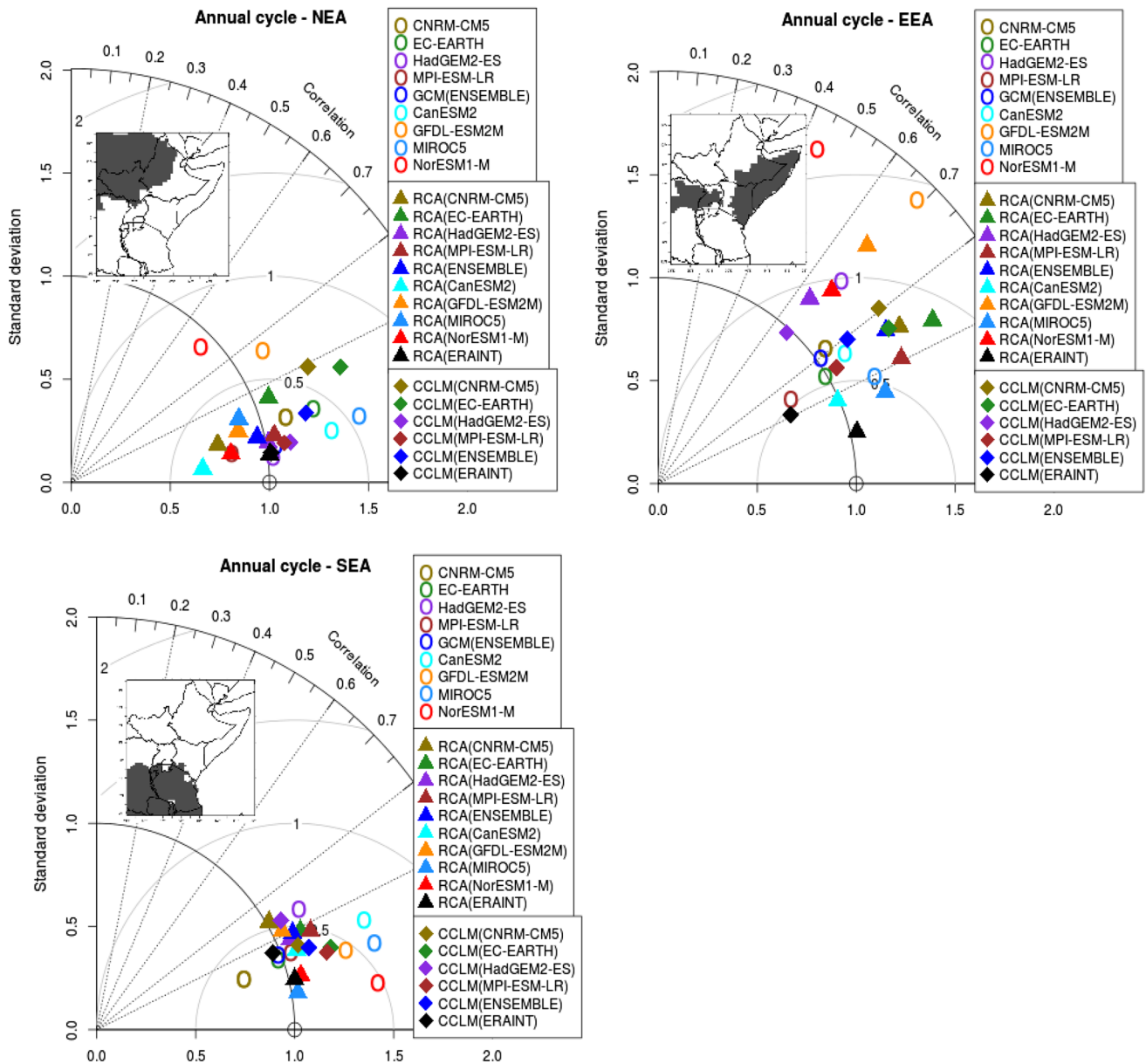
Fig. 7 Taylor diagram quantifying the correspondence between the simulated and observed area-averaged annual cycle of rainfall in each homogeneous rainfall sub-regions. *Circles* are for GCMs, *triangles* are for RCA and *diamonds* for CCLM model

A similar approach is used to identify the IOD years. IOD years are identified using the DMI (Saji et al. 1999), which is calculated as the SST anomaly difference between the western equatorial Indian Ocean (50°–70°E and 10°S–10°N) and south-eastern equatorial Indian Ocean (90°–110°E and 10°–0°S). Like ONI, this index oscillates between positive and negative values. A given year is defined as positive IOD or negative IOD year when DMI index is higher (lower) than a positive (negative) threshold for at least three consecutive overlapping seasons including OND, defined as the average of three consecutive months of that year. Note that for IOD we used 3 consecutive

seasons including OND, since an IOD usually starts in May or June, peaks between August and November and then rapidly decays. For observation, a threshold ±0.5 °C is used to identify positive IOD and negative IOD years, while for CGCMs (similar to the ENSO) the thresholds are based the their respective Sd of DMI. Number of ENSO and IOD years for an observation dataset (NOAA_OI_SST_V2) and each CGCM and the corresponding standard deviation (SD) of ONI and DMI indices are presented in Table 2.

The rainfall anomalies over the region associated with ENSO and IOD from composite analysis are similar to

Table 2 Number of ENSO (El Niño and La Niña) and IOD (Positive IOD and Negative IOD) years, and the corresponding standard deviations (Sd) in the 1982–2005 period

Obs and CGCMs	ONI Sd	El Niño	La Niña	DMI Sd	+ve IOD	−ve IOD
NOAA_OI_SST_V2	1.07	8	6	0.62	4	7
CNRM-CM5	0.98	9	7	0.62	8	8
EC-EARTH	0.72	6	7	0.45	5	9
HadGEM2-ES	0.87	8	6	0.58	8	6
MPI-ESM-LR	1.27	5	6	0.65	3	5
CanESM2	1.13	6	8	0.49	7	8
GFDL-ESM2M	1.66	5	8	0.76	5	7
MIROC5	1.42	7	7	0.63	4	8
NorESM1-M	0.88	7	9	0.57	6	7

those obtained using regression analysis (Fig. 5), so our subsequent analyses will concentrate only on circulation anomalies associated with ENSO and IOD. Moreover, the climatological pattern of SLP and 850 hPa wind over eastern Africa for JJAS and OND are discussed in part I of our paper (see Endris et al. 2013). Figure 8a shows the El Niño anomalies of SLP and 850 hPa wind vectors for RCMs and their driving CGCMs in comparison with ERA-Interim reanalysis. ERA-Interim (our reference data in this case) shows strong positive SLP anomalies over the Arabian Peninsula. The positive SLP anomalies over Arabian Peninsula reflect the weakening of the monsoon through during El Niño. As Diro et al. (2011b) described, the weakening of monsoon trough over Arabian Peninsula might reduce the east–west pressure gradient, and consequently reduce the westerly winds from Atlantic/Congo, and leads to reduction of rainfall over the northern part of the region during JJAS. It also become evident that there is a reduction of the Somali Low Level Jets (SLLJ) diverging out of the Mascarene high, and the strength of westerly winds from the South Atlantic high, which are the main sources of moisture over the northern part of the domain during JJAS. The reduction of these winds is manifested by the presence of north-easterly wind anomaly vectors off the coast of East Africa, and easterly wind anomaly vectors over western part of Eastern Africa. In contrast, during La Niña (figure not shown) most part of the study region is dominated by negative SLP anomalies particularly with deepening of the trough over the Arabian Peninsula. The deeper monsoon trough over the Arabian area is strongly associated with greater rainfall over the eastern Africa during JJAS. In addition, there are anomalies of strong westerly wind vectors as result of SLP intensification over the Atlantic basin, and south-easterly wind vectors as a result of SLP intensification over the Indian Ocean, which produce abundant rainfall over the region. These finds are consistent with findings of other studies such as Segele and Lamb (2005), Segele et al. (2009a, b), Diro et al. (2011b).

Some models represent the intensity as well as the spatial pattern of circulation anomalies associated with El

Niño and La Niña; particularly the ERA-Interim driven RCMs, Ensemble mean, HadGEM2-ES and its corresponding downscaled results. Consistent with the rainfall results shown in Fig. 5, the two RCMs driven by CNRM-CM5 show opposite anomaly circulation patterns in comparison with the reanalysis. These models show negative SLP anomalies over east coast of Africa and zero SLP anomalies over the Arabian Peninsula (Fig. 8a). They also show an easterly and south-easterly wind vector anomalies, opposite to the reanalysis. Even though these patterns were not observed in the forcing CGCM (CNRM-CM5), analysis of the CNRM-CM5 model patterns over the large domain (15°W–120°E and 35°S–35°N) showed strong negative (positive) SLP anomalies during El Niño (La Niña) over the northern part of Africa (over Algeria, Tunisia and Libya), which has not been observed in the reanalysis. We expect that this wrong signal in the driving CGCM might be transferred to the RCMs, which leads the RCMs to generate a wrong anomalous circulation patterns over the domain. MPI-ESM-LR and its corresponding downscaled results show more intense SLP and wind field anomalies than ERA-Interim over the Arabian area extended down to western part of the Indian Ocean, while EC-EARTH model shows strong positive anomalies of SLP over western part of the Indian Ocean rather than over the Arabian Peninsula. The anomalous troughs over south Sudan represented by NorESM1-M, RCA (MIROC5) and RCA (NorESM1-M) are not seen in the reanalysis.

During OND, interannual rainfall variability over Eastern Africa is linked to both ENSO and IOD (Fig. 5b, c; Clark et al. 2003; Hasternrath 2007; Bahaga et al. 2015 and others). In general, the southern and equatorial part of Eastern Africa receives above normal rainfall during El Niño and positive IOD, and below normal during La Niña and negative IOD. To highlight the underlining mechanisms linking the ENSO and IOD with Eastern African rainfall, and also to evaluate the ability of the models to reproduce the anomalous circulation patterns, the composite SLP and 850 wind fields are analyzed. The regional patterns for La Niña (negative IOD) are generally opposite-signed anomalies to
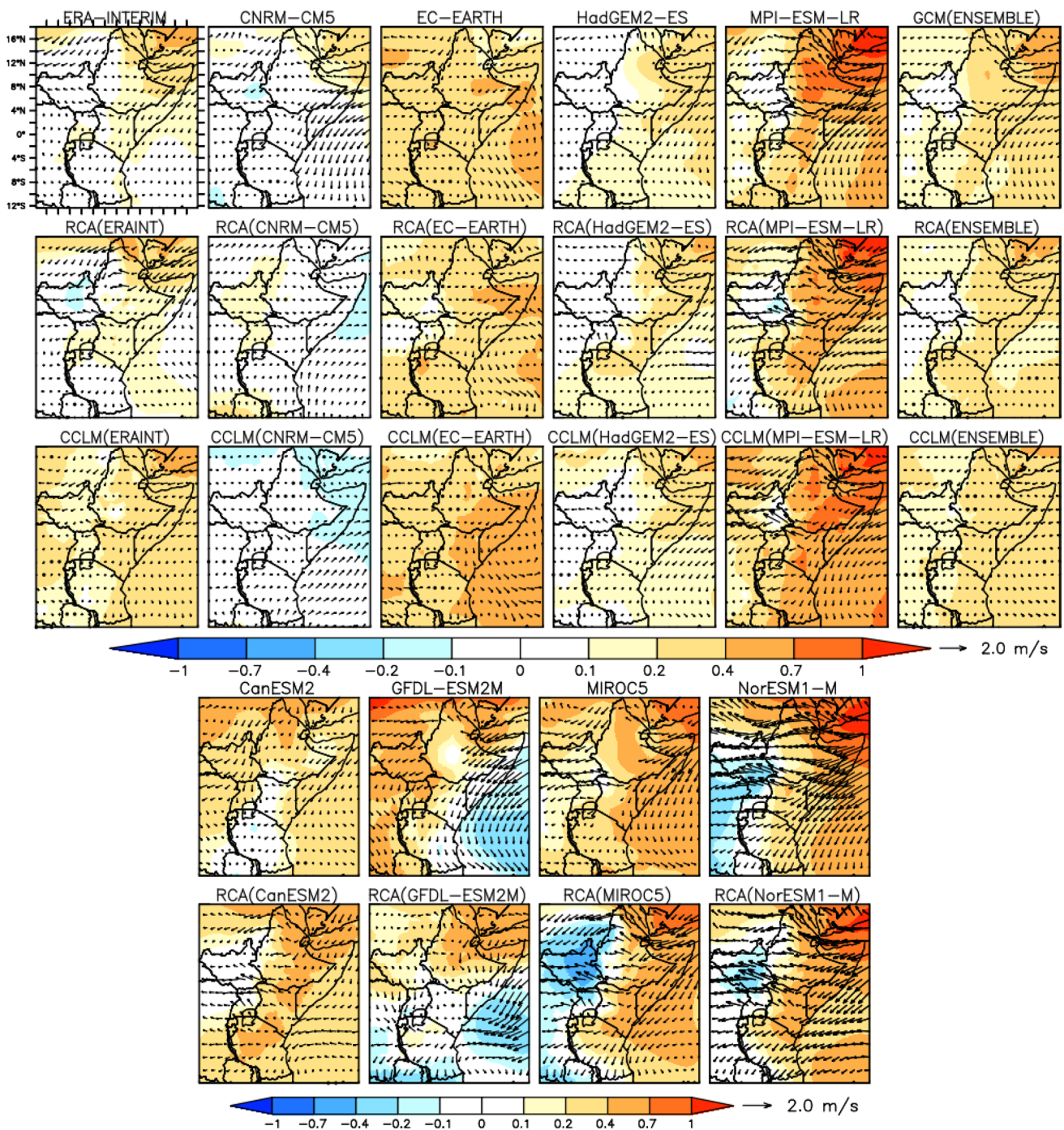
Fig. 8 **a** JJAS El Nino anomalies of SLP (*shaded* in hPa) and 850 hPa winds (*vectors* in m/s). **b** OND El Nino anomalies of SLP (*shaded* in hPa) and 850 hPa winds (*vectors* in m/s). **c** OND positive IOD anomalies of SLP (*shaded* in hPa) and 850 hPa winds (*vectors* in m/s)

El Niño (positive IOD), thus our analysis will concentrate only on anomalous circulation patterns associated with El Niño and positive IOD events. Figure 8b shows the SLP and 850 hPa wind vector anomalies associated with El Niño. Positive surface pressure anomalies are observed over the western part of Eastern Africa, and negative surface pressure anomalies are observed over the south-western part

of the Indian Ocean. Moreover, westerly wind anomalies observed over the western part of the domain, and easterly anomalies over the western equatorial Indian Ocean. Kijazi and Reason (2005) link the wet conditions during El Niño events to easterly anomalies over the western equatorial Indian Ocean, while other studies (e.g. Latif et al. 1999; Black et al. 2003) have proposed that the relationship
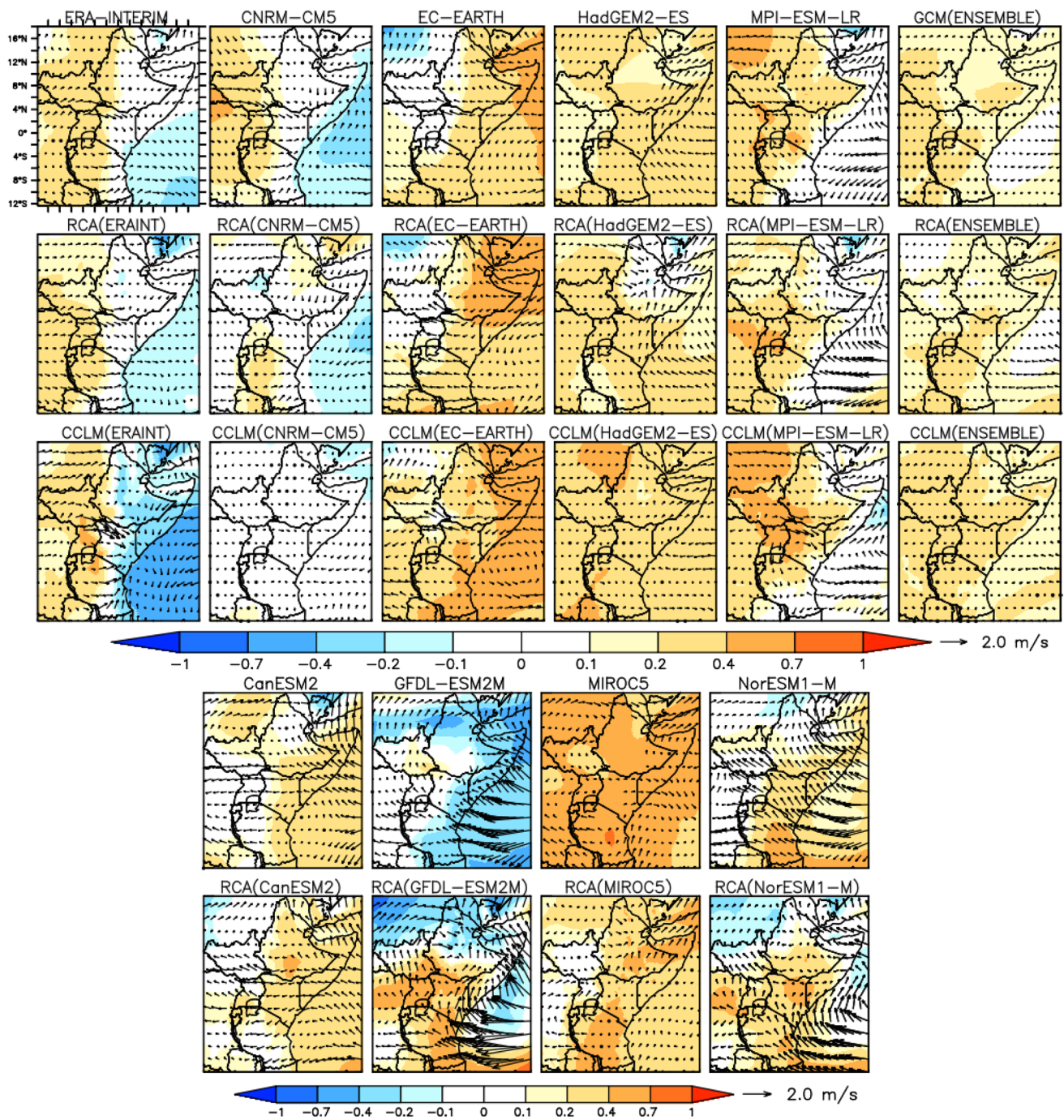
Fig. 8 continued

between East African rainfall and ENSO as the result of an indirect forcing by ENSO on the Indian Ocean. Some of the models are able reproduce the observed anomaly circulation patterns. However, consistent with the rainfall anomalies in Fig. 5b, EC-EARTH, CanESM2, MIROC5 and their corresponding downscaled results fail to represent the negative SLP anomalies over the western tropical Indian Ocean. The models GFDL-ESM2M and NorESM1-M and their

corresponding downscaled results show more intense easterly wind anomalies towards Eastern Africa. Overall, there is a clear effect of the CGCM-supplied boundary conditions in simulating the local anomalous circulation patterns, and the error from boundary conditions can be summarized as the "garbage in/garbage out problem".

During positive IOD, there are positive SLP anomalies over the west of Eastern Africa and negative anomalies over
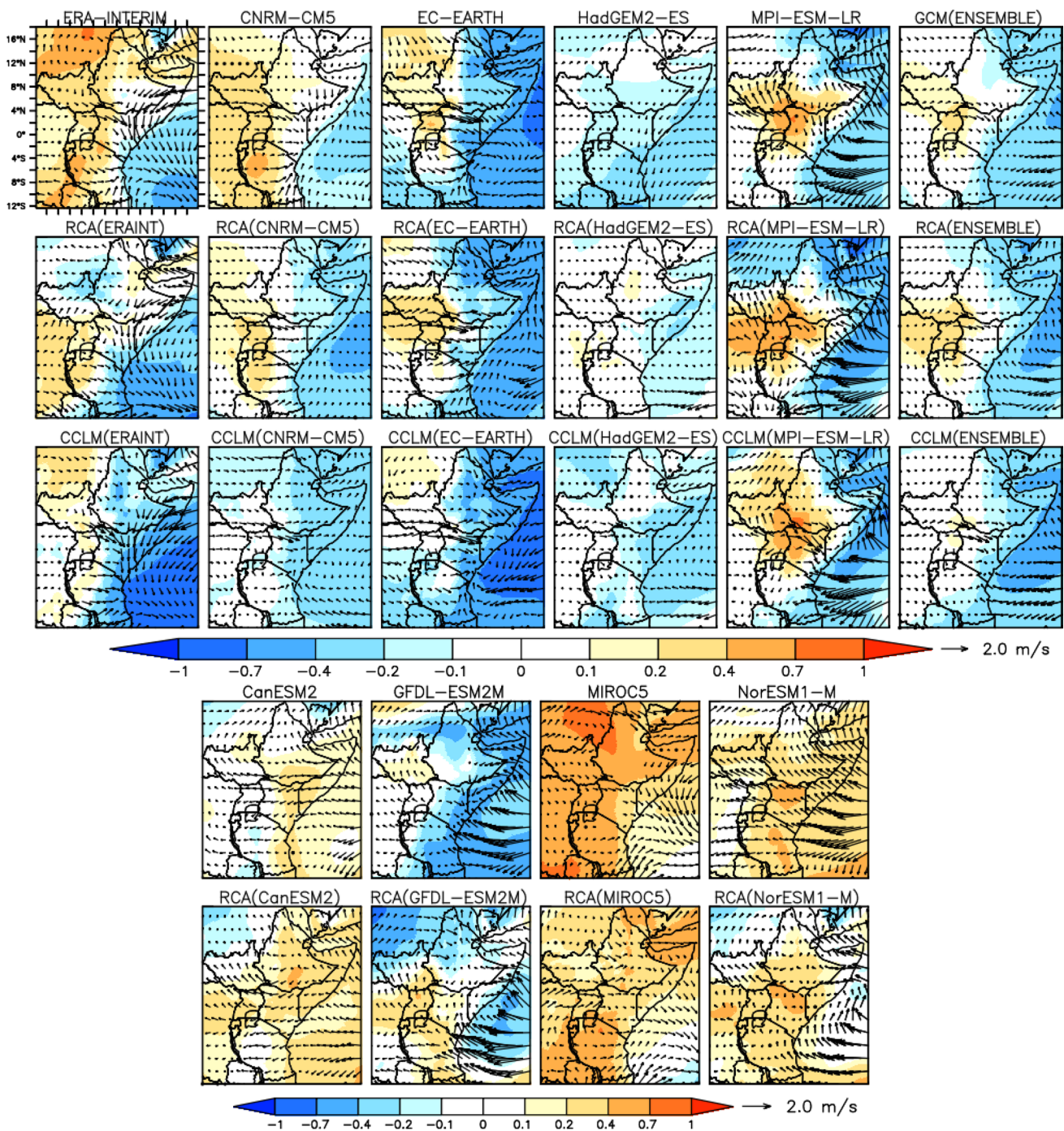
Fig. 8 continued

the western part of the Indian Ocean (see Fig. 8c). The negative SLP anomalies are associated with the warming of the western part of the Ocean during its positive phase. Consistent with the surface pressure response, there are westerly 850 hPa wind anomalies over west of Eastern Africa, and strong easterly anomalies (associated with the cold SST over eastern tropical Indian Ocean) off the east coast of Somalia. These two anomalies converge along the equator and generate north-westerly wind anomalies moving towards the south-east Indian Ocean. Even though the positive (negative) IOD events are linked with above (below) normal rainfall over equatorial and southern part of eastern Africa during OND, the mechanisms for this teleconnection (response of rainfall to anomalous circulation) are not quite clear yet. Ummenhofer et al. (2009) suggested that a reduction in sea level pressure over the western half of the Indian Ocean and

converging wind anomalies over Eastern Africa lead to moisture convergence and increase convective activity over the region during its positive phase. However, Begeha (2014) emphasizes the role of the westerly flows from Congo air mass and the Atlantic region as the main moisture sources for the increase on rainfall over the region. We focus on the ability of the models in reproducing the observed anomalous circulation features. It appears that most models capture the observed broad-scale anomalous circulation characteristics associated with a positive IOD using ERA-Interim as reference, though some models exhibit some variations from the patterns observed. Particularly, CanESM2, MIROC5 and NorESM2-M again misrepresent the negative SLP anomalies associated with warm SST over western tropical Indian Ocean. We argue that this significant short-coming from these CGCMs suggests strongly that these three models are unable to represent the potential implications of circulation pattern change in Eastern Africa.

4 Summary and conclusions

Climate variability is an important aspect of regional climate so assessing the ability of climate models to simulate the natural climate variability of a region is an essential task of evaluating these models. An important component/driver of climate variability over many regions of the world is the SST-rainfall teleconnection. This study examines the ability of two CORDEX RCMs and their driving CGCMs to capture SST-rainfall teleconnection patterns over Eastern Africa. The regional models used in the study are RCA driven by eight CGCMs and CCLM driven by four of common CGCMs. The reanalysis-driven simulations from the two RCMs are also analyzed to estimate error produced by the RCMs and those transmitted from driving CGCMs. We conduct the assessment over three homogeneous rainfall sub-regions, which cover most of Eastern Africa, namely: NEA, EEA and SEA. The analysis period is from 1982 to 2005, which is the period that observed data are available.

Spearman's rank correlation, linear regression and composite analysis were used to examine the teleconnections patterns. The Spearman's rank correlation is used to identify oceanic regions that have a robust relationship with regional rainfall, and also to assess the models' ability to simulate the spatial pattern of the teleconnection patterns. Linear regression is applied to evaluate the ability of models to simulate both the patterns and the amplitude of rainfall teleconnections over the region against different SST indices in Oceanic regions that have strong correlations with Eastern African rainfall. Composite analysis was employed to assess the models' ability to represent the anomalous circulation patterns associated with the dominant modes affecting the rainfall over the region.

The results show that some models reproduce the observed teleconnective SST-rainfall patterns (spatial patterns and amplitudes) better than others. The downscaled RCM-reanalysis runs are in better agreement with observation than RCM–CGCM runs in most of the examined sub-regions and seasons. Generally, RCMs driven by MPI-ESM-LR, HadGEM2-ES and GFDL-ESM2M performed better than RCMs driven by other CGCMs. CanESM2 and MIROC5, and their corresponding downscaled results capture the teleconnections in most of the sub-regions and seasons poorly. CGCMs generally underestimate the amplitude of teleconnection patterns while RCMs tend to overestimate it. The overestimation of amplitude by the RCMs is likely because of enhanced precipitation due to a better-resolved topography. It is also demonstrated that both the CGCMs and corresponding downscaled results exhibit a similar teleconnection pattern over regions where the rainfall is primarily controlled by large-scale features, with the RCMs maintaining the overall regional patterns from the forcing models. Differences in RCM simulations from corresponding driving simulations are noted mainly over northern part of the domain which is most likely related to mesoscale processes that are not resolved by CGCMs.

The models' performance in reproducing the large-scale anomalies in SLP and low-level winds are consistent with their performance at representing the rainfall anomalies. The ERA-Interim driven simulations produce a more realistic representation in the magnitude of these fields. Consistent with the rainfall anomalies, CanESM2 and MIROC5 and their corresponding downscaled results fail to represent anomalous circulation patterns associated with ENSO and IOD in most of the examined regions and seasons. So we suggest that it's not only the parameterizations in the RCMs that are the cause of the errors in the downscaled rainfall fields, the driving circulation states were not captured, as CGCM-derived boundary conditions were incorrect. We would also like to note that the simulation domain is much bigger than the study region giving the RCMs gives a lot of freedom to develop its own climate. Despite this the RCMs cannot improve on the CGCM results over the region if the CGCM boundary conditions are poor.

In conclusion, the results of this study demonstrate that differences in reproducing SST-rainfall teleconnection patterns arise mainly from the driving CGCMs. In other words, the relative contribution of teleconnection errors from boundary forcing is bigger than the choice of RCM or RCM configuration, implying that the choice of the forcing CGCM is more important than the choice of the RCM for the regional application. We suggest that more work should be targeted towards improving the boundary forcing given to the RCMs. We further suggest that the analysis presented here is helpful in selecting the appropriate models for regional applications over the Eastern Africa region. In

future work, we aim to investigate whether the current teleconnection patterns between the large scale climate modes (ENSO and IOD) and rainfall over Eastern Africa will persist in the future under anthropogenic climate change.

References

Abram NJ, Gagan MK, Cole JE, Hantoro WS, Mudelsee M (2008) Recent intensification of tropical climate variability in the Indian Ocean. Nat Geosci 1(12):849–853

Anyah RO, Semazzi FH (2007) Variability of East African rainfall based on multiyear RegCM3 simulations. Int J Climatol 27(3):357–371

Bahaga TK, Mengistu Tsidu G, Kucharski F, Diro GT (2015) Potential predictability of the sea-surface temperature forced equatorial East African short rains interannual variability in the 20th century. Quarterly J R Meteorol Soc 141(686):16–26

Baldauf M, Seifert A, Förstner J, Majewski D, Raschendorfer M, Reinhardt T (2011) Operational convective-scale numerical weather prediction with the COSMO model: description and sensitivities. Mon Weather Rev 139(12):3887–3905

Behera SK, Luo JJ, Masson S, Delecluse P, Gualdi S, Navarra A, Yamagata T (2005) Paramount impact of the Indian Ocean dipole on the East African short rains: A CGCM study. J Clim 18(21):4514–4530

Black E, Slingo J, Sperber KR (2003) An observational study of the relationship between excessively strong short rains in coastal East Africa and Indian Ocean SST. Mon Weather Rev 131(1):74–94

Bland JM, Altman DG (1995) Multiple significance tests: the Bonferroni method. BMJ 310(6973):170

Boulard D, Pohl B, Crétat J, Vigaud N, Pham-Xuan T (2013) Downscaling large-scale climate variability using a regional climate model: the case of ENSO over Southern Africa. Clim Dyn 40(5–6):1141–1168

Clark CO, Webster PJ, Cole JE (2003) Interdecadal variability of the relationship between the Indian Ocean zonal mode and East African coastal rainfall anomalies. J Clim 16(3):548–554

Da Rocha RP, Reboita MS, Dutra LMM, Llopart MP, Coppola E (2014) Interannual variability associated with ENSO: present and future climate projections of RegCM4 for South America-CORDEX domain. Clim Change. doi:10.1007/s10584-014-1119-y

Dee DP, Uppala SM, Simmons AJ, Berrisford P, Poli P, Kobayashi S, Andrae U, Vitart F (2011) The ERA-Interim reanalysis: configuration and performance of the data assimilation system. Q J R Meteorol Soc 137(656):553–597

Déqué M, Piedelievre JP (1995) High resolution climate simulation over Europe. Clim Dyn 11(6):321–339

Diro GT, Grimes DIF, Black E (2011a) Large scale features affecting Ethiopian rainfall. In: Williams CJR, Kniveton DR (eds) African climate and climate change, Springer, Netherlands pp 13–50

Diro GT, Grimes DIF, Black E (2011b) Teleconnections between Ethiopian summer rainfall and sea surface temperature: part I—observation and modelling. Clim Dyn 37(1–2):103–119

Dosio A, Panitz H-J (2015) Dynamically downscaling of CMPI5 CGMs over CORDEX-Africa with COSMO-CLM: analysis of the climate change signal and differences with the driving GCMs. Clim Dyn. doi:10.1007/s00382-015-2664-4

Dosio A, Panitz H-J, Schubert-Frisius M, Luethi D (2015) Dynamical downscaling of CMIP5 global circulation models over CORDEX-Africa with COSMO-CLM: evaluation over the present climate and analysis of the added value. Clim Dyn 44:2637–2661. doi:10.1007/s00382-014-2262-x

Endris HS, Omondi P, Jain S, Lennard C, Hewitson B, Chang'a L, Awange JL, Tazalika L (2013) Assessment of the performance of CORDEX regional climate models in simulating East African rainfall. J Clim 26(21):8453–8475

Enfield DB, Mestas-Nuñez AM, Mayer DA, Cid-Serrano L (1999) How ubiquitous is the dipole relationship in tropical Atlantic sea surface temperatures? Journal of Geophysical Research: Oceans (1978–2012) 104(C4):7841–7848

FEWS NET (2011) Past year one of the driest on record in the eastern Horn. Famine early warning system network report, June 14, 2011, U.S. Agency for International Development, Washington, DC

Fox-Rabinovitz M, Côté J, Dugas B, Déqué M, McGregor JL (2006) Variable resolution generalcirculation models: Stretched-grid model intercomparison project (SGMIP). J Geophys Res 111:D16104. doi:10.1029/2005JD006520

Giorgi F, Mearns LO (1991) Approaches to the simulation of regional climate change: a review. Rev Geophys 29(2):191–216

Giorgi F, Mearns LO (1999) Introduction to special section: regional climate modeling revisited. J Geophys Res Atmos (1984–2012) 104(6):6335–6352

Giorgi F, Christensen J, Hulme M, Von Storch H, Whetton P, Jones R, Mearns L, Semazzi F (2001) Regional climate information-evaluation and projections. In: Houghton JT et al (eds) Climate change 2001: the scientific basis. Contribution of working group to the third assessment report of the intergovernmental panel on climate change. Cambridge University Press, Cambridge

Giorgi F, Jones C, Asrar GR (2009) Addressing climate information needs at the regional level: the CORDEX framework. World Meteorol Organ (WMO) Bull 58(3):175

Gissila T, Black E, Grimes DIF, Slingo JM (2004) Seasonal forecasting of the Ethiopian summer rains. Int J Climatol 24(11):1345–1358

Hastenrath S (2007) Circulation mechanisms of climate anomalies in East Africa and the equatorial Indian Ocean. Dyn Atmos Oceans 43(1):25–35

Hauke J, Kossowski T (2011) Comparison of values of Pearson's and Spearman's correlation coefficients on the same sets of data. Quaest Geogr 30(2):87–93

Hewitson B, Crane R (1996) Climate downscaling: techniques and application. Clim Res 7:85–95. doi:10.3354/cr007085

Indeje M, Semazzi FH, Ogallo LJ (2000) ENSO signals in East African rainfall seasons. Int J Climatol 20(1):19–46

Intergovernmental Panel on Climate Change (IPCC) (2007) Climate change 2007-the physical science basis: Working group I contribution to the fourth assessment report of the IPCC (S Solomon et al (eds)). Cambridge University Press

Intergovernmental Panel on Climate Change (IPCC) (2013) Climate change 2013: the physical science basis. In: Contribution of working group i to the fifth assessment report of the intergovernmental panel on climate change, T F Stocker, D Qin, G-K Plattner, M Tignor, S K Allen, J Boschung, et al (eds) (Cambridge, New York: Cambridge University Press), p 1535

Kalognomou EA, Lennard C, Shongwe M, Pinto I, Favre A, Kent M, Büchner M (2013) A diagnostic evaluation of precipitation in

CORDEX models over Southern Africa. J Clim 26:9477–9506. doi:10.1175/JCLI-D-12-00703.1

Kijazi AL, Reason CJC (2005) Relationships between intraseasonal rainfall variability of coastal Tanzania and ENSO. Theor appl climatol 82(3–4):153–176

Kim J, Waliser DE, Mattmann CA, Goodale CE, Hart AF, Zimdars PA, Favre A (2014) Evaluation of the CORDEX-Africa multi-RCM hindcast: systematic model errors. Clim dyna 42(5-6):1189–1202

Kosaka Y, Xie SP (2013) Recent global-warming hiatus tied to equatorial Pacific surface cooling. Nature 501(7467):403–407

Langenbrunner B, Neelin JD (2013) Analyzing enso teleconnections in cmip models as a measure of model fidelity in simulating precipitation. J Clim 26:4431–4446. doi:10.1175/JCLI-D-12-00542.1

Latif M, Dommenget D, Dima M, Grötzner A (1999) The role of Indian Ocean sea surface temperature in forcing east African rainfall anomalies during December-January 1997/98. J Clim 12(12):3497–3504

Liebmann B, Bladé I, Kiladis GN, Carvalho LMV, Senay GB, Allured D, Funk C (2012) Seasonality of African precipitation from 1996 to 2009. J Clim 25:4304–4322. doi:10.1175/JCLI-D-11-00157.1

Mason SJ, Goddard L (2001) Probabilistic precipitation anomalies associated with ENSO. Bull Am Meteorol Soc 82(4):619–638

Murtagh F (1985) Multidimensional clustering algorithms. In: Chambers JM, Gordesch J, Klas A, Lebart L, Sint PP (eds) Compstat lectures, Würzburg: Physica-Verlag, Vienna

Nicholson SE, Kim J (1997) The relationship of the El Nino-Southern oscillation to African rainfall. Int J Climatol 17(2):117–135

Nikulin G, Jones C, Giorgi F, Asrar G, Büchner M, Cerezo-Mota R, Hänsler A, Sushama L (2012) Precipitation climatology in an ensemble of CORDEX-Africa regional climate simulations. J Clim 25(18):6057–6078

Ogallo LJ (1988) Relationships between seasonal rainfall in East Africa and the Southern oscillation. J Climatol 8(1):31–43

Paeth H, Hall NM, Gaertner MA, Alonso MD, Moumouni S, Polcher J, Ruti PM, Rummukainen M (2011) Progress in regional downscaling of West African precipitation. Atmos Sci Lett 12(1):75–82

Panitz HJ, Dosio A, Büchner M, Lüthi D, Keuler K (2014) COSMO-CLM (CCLM) climate simulations over CORDEX-Africa domain: analysis of the ERA-Interim driven simulations at 0.44 and 0.22 resolution. Clim Dyn 42(11–12):3015–3038

Reynolds RW, Rayner NA, Smith TM, Stokes DC, Wang WQ (2002) An improved in situ and satellite SST analysis for climate. J Clim 15:1609–1625

Ropelewski CF, Halpert MS (1987) Global and regional scale precipitation patterns associated with the El Niño/Southern Oscillation. Mon Weather Rev 115(8):1606–1626

Rowell DP (2013) Simulating SST teleconnections to Africa: What is the state of the art?. J Clim 26(15):5397–5418

Rudolf B, Becker A, Schneider U, Meyer-Christoffer A, Ziese M (2010) The new "GPCC full data reanalysis version 5" providing high-quality gridded monthly precipitation data for the global land-surface is public available since December 2010. GPCC status report December

Rummukainen M (2010) State-of-the-art with regional climate models. Wiley Interdiscip Rev Clim Change 1(1):82–96

Saji NH, Goswami BN, Vinayachandran PN, Yamagata T (1999) A dipole mode in the tropical Indian Ocean. Nature 401(6751):360–363

Samuelsson P, Jones CG, Willén U, Ullerstig A, Gollvik S, Hansson U, Kjellström E, Nikulin G, Wyser K (2011) The Rossby centre regional climate model RCA3: model description and performance. Tellus A 63:4–23

Segele ZT, Lamb PJ (2005) Characterization and variability of Kiremt rainy season over Ethiopia. Meteorol Atmos Phys 89(1–4):153–180

Segele ZT, Lamb PJ, Leslie LM (2009a) Large-scale atmospheric circulation and global sea surface temperature associations with Horn of Africa June–September rainfall. Int J Climatol 29(8):1075–1100

Segele ZT, Leslie LM, Lamb PJ (2009b) Evaluation and adaptation of a regional climate model for the Horn of Africa: rainfall climatology and interannual variability. Int J Climatol 29(1):47–65

Slim H (2012) IASC real-time evaluation of the humanitarian response to the horn of africa drought crisis in Somalia, Ethiopia and Kenya. Available from: http://reliefweb.int/sites/reliefweb.int/files/resources/RTE_HoA_SynthesisReport_FINAL.pdf

Sylla MB, Gaye AT, Pal JS, Jenkins GS, Bi XQ (2009) High-resolution simulations of West African climate using regional climate model (RegCM3) with different lateral boundary conditions. Theoret Appl Climatol 98(3–4):293–314

Taylor KE (2001) Summarizing multiple aspects of model performance in a single diagram. J Geophys Res 106(D7):7183–7192

Taylor KE, Stouffer RJ, Meehl GA (2012) An overview of CMIP5 and the experiment design. Bull Am Meteorol Soc 93(4):485–498

Tourigny E, Jones CG (2009) An analysis of regional climate model performance over the tropical Americas. Part I: simulating seasonal variability of precipitation associated with ENSO forcing. Tellus A 61(3):323–342

Ummenhofer CC, Sen Gupta A, England MH, Reason CJ (2009) Contributions of Indian Ocean sea surface temperatures to enhanced East African rainfall. J Clim 22(4):993–1013

United Nations Office for the Coordination of Humanitarian Affairs (UNOCHA) (2011) Eastern Africa drought humanitarian report 4, 15 July, New York, NY

Wang Y, Leung LR, McGREGOR JL, Lee DK, Wang WC, Ding Y, Kimura F (2004) Regional climate modeling: progress, challenges, and prospects. J Meteorol Soc Jpn 82:1599–1628

Yang SC, Keppenne C, Rienecker M, Kalnay E (2009) Application of coupled bred vectors to seasonal-to-interannual forecasting and ocean data assimilation. J Clim 22(11):2850–2870